INTERFACE

royalsocietypublishing.org/journal/rsif

Research

Cite this article: Tun WM *et al*. 2021 A massively multi-scale approach to characterizing tissue architecture by synchrotron micro-CT applied to the human placenta. *J. R. Soc. Interface* **18**: 20210140. https://doi.org/10.1098/rsif.2021.0140

Received: 16 February 2021
Accepted: 6 May 2021

Subject Category:
Life Sciences–Engineering interface

Subject Areas:
bioengineering, computational biology, biomedical engineering

Keywords:
human placenta, computed tomography, contrast agent, machine-learning segmentation, flow network, spatial statistics

Authors for correspondence:
P. Brownbill
e-mail: paul.brownbill@manchester.ac.uk
M. Darrow
e-mail: michele.c.darrow@gmail.com
I. L. Chernyavsky
e-mail: igor.chernyavsky@manchester.ac.uk

†These authors contributed equally to this work.
‡Joint lead authors.

Electronic supplementary material is available online at https://doi.org/10.6084/m9.figshare.c.5428744.

THE ROYAL SOCIETY PUBLISHING

A massively multi-scale approach to characterizing tissue architecture by synchrotron micro-CT applied to the human placenta

W. M. Tun[1,†], G. Poologasundarampillai[2,†], H. Bischof[3,4], G. Nye[5], O. N. F. King[1], M. Basham[1,6], Y. Tokudome[7], R. M. Lewis[8], E. D. Johnstone[3,4], P. Brownbill[3,4,‡], M. Darrow[9,‡] and I. L. Chernyavsky[3,4,10,‡]

[1]Diamond Light Source, Didcot OX11 0DE, UK
[2]School of Dentistry, University of Birmingham, Birmingham B15 2TT, UK
[3]Maternal and Fetal Health Research Centre, School of Medical Sciences, University of Manchester, Manchester, UK
[4]MAHSC, St Mary's Hospital, NHS MFT, Manchester M13 9WL, UK
[5]Chester Medical School, University of Chester, Chester CH1 4BJ, UK
[6]Rosalind Franklin Institute, Didcot OX11 0DE, UK
[7]Department of Materials Science, Graduate School of Engineering, Osaka Prefecture University, Osaka 599-8531, Japan
[8]Faculty of Medicine, University of Southampton, Southampton SO16 6YD, UK
[9]SPT Labtech Ltd, Melbourn SG8 6HB, UK
[10]Department of Mathematics, University of Manchester, Manchester M13 9PL, UK

WMT, 0000-0003-0991-8785; GP, 0000-0002-8498-323X; ONFK, 0000-0002-6152-7207; MB, 0000-0002-8438-1415; RML, 0000-0003-4044-9104; PB, 0000-0002-8328-7072; MD, 0000-0001-6259-1684; ILC, 0000-0003-0284-9318

Multi-scale structural assessment of biological soft tissue is challenging but essential to gain insight into structure–function relationships of tissue/organ. Using the human placenta as an example, this study brings together sophisticated sample preparation protocols, advanced imaging and robust, validated machine-learning segmentation techniques to provide the first massively multi-scale and multi-domain information that enables detailed morphological and functional analyses of both maternal and fetal placental domains. Finally, we quantify the scale-dependent error in morphological metrics of heterogeneous placental tissue, estimating the minimal tissue scale needed in extracting meaningful biological data. The developed protocol is beneficial for high-throughput investigation of structure–function relationships in both normal and diseased placentas, allowing us to optimize therapeutic approaches for pathological pregnancies. In addition, the methodology presented is applicable in the characterization of tissue architecture and physiological behaviours of other complex organs with similarity to the placenta, where an exchange barrier possesses circulating vascular and avascular fluid spaces.

1. Introduction

Understanding complex vascular-rich organs such as the placenta has traditionally necessitated the adoption of multiple parallel imaging-based approaches, applied correlatively to gain structural and functional understanding of the tissue. These approaches generally require balancing resolution with sample volume. Structural analyses of placental vessels from the whole organ or single villous branches have been conducted using multiple imaging modalities [1,2] including computed tomography (CT) angiography [3], micro-CT [4,5], confocal laser scanning microscopy (CLSM) [6] and fluorescent CLSM [7]. Each of these methods has positives and negatives associated with it; however,

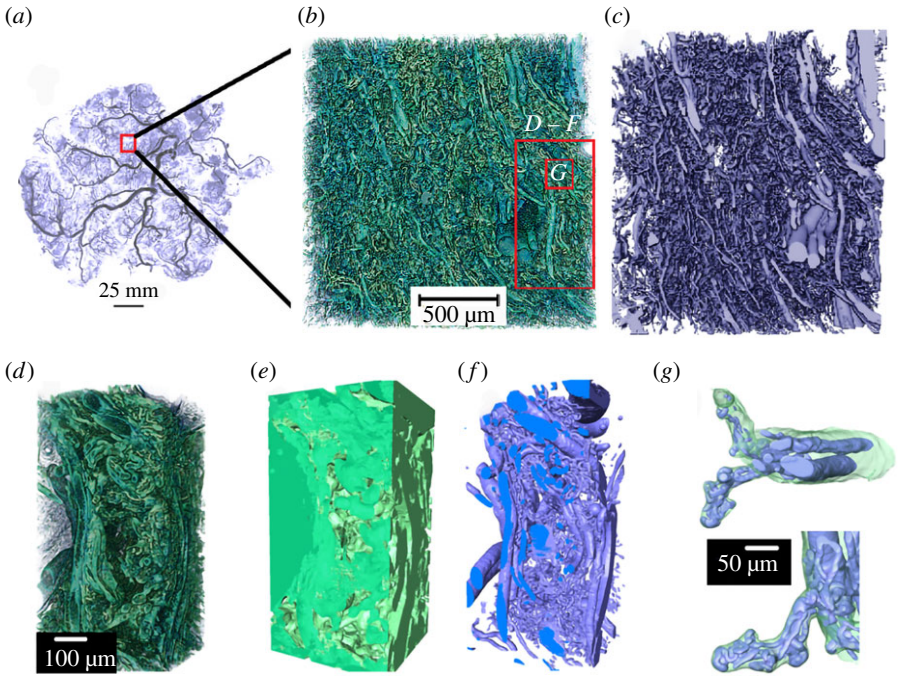

Figure 1. Multi-scale tissue architecture of placental tissue from synchrotron micro-CT. (*a*) Placental cast under micro-CT (unpublished image from [5]). (*b–g*) Images demonstrating the complex hierarchical architecture of the human placenta (Specimen 1, normal placenta at term). (*b*) Three-dimensional rendering of approximately 8 mm^3 human placental tissue. (*c*) Fetal vascular network segmented from placental tissue using a U-Net algorithm. (*d–f*) A small section of the placental tissue was cropped from the original dataset (red box in *b*) and 3D rendered. (*d*) Three-dimensional rendering of approximately 0.2 mm^3 tissue showing different hierarchical features. (*e*) U-Net segmented fetal tissue component, (*f*) fetal vessels and (*g*) fetal capillary network with surrounding villous tissue overlaid.

none of them provide access to three-dimensional (3D) microstructures *in situ*, at high enough resolution to resolve the blood vessels, or functional units of the placenta, and still provide contextual information of the tissue.

Segmenting biological image data is a major challenge due to the structural complexity and intra/inter sample heterogeneity [8,9]. Manual segmentation is commonly used for biological data segmentation; however, as the number and size of datasets increases, this approach has become increasingly impractical [10]. Thus, an automatic or semi-automatic segmentation algorithm with high accuracy is required for high-throughput segmentation of biological structure.

As one of the most complex vascular organs of the human body, the placenta is a well-suited model system for development of 3D imaging pipelines. The human placenta is an exchange organ with a large surface area of the feto-maternal interface packed in a relatively small volume, and an extensive feto-placental vascular network [11]. Its tightly integrated structural constituents span the spatial range from approximately 10^{-6} to 10^{-1} m, necessitating a truly massive multi-scale imaging modality. Thus, new experimental and theoretical approaches are needed to bridge the microstructure of the placental exchange barrier and its macroscopic organ-level function, including the 3D characterization of the mesoscopic (between approx. 0.1 and 1 mm) tissue domain [1,11].

In this study, synchrotron X-ray imaging is used in combination with various sample processing conditions, including tissue contrast agents, vascular cast resins, fixation and embedding methods to generate high-resolution massively multi-scale datasets of the human placenta. We then apply machine learning-based segmentation techniques for robust and efficient decomposition of maternal and fetal micro-domains in the large (approx. 8 mm^3) datasets. Finally, spatial statistics and flow simulations of the feto-placental vascular network and associated intervillous porous space of the placental tissue are presented, and the results are validated against other modalities such as traditional two-dimensional (2D) stereology analysis and *in vivo* magnetic resonance imaging.

The developed protocols for 3D multi-domain characterization of tissues presented here, using the human placenta as an example, will enable more direct hypothesis testing of the structure–function relationship in other organs where there are complex physiological fluidic/exchanger systems, such as in the kidney, lung, lymphatics, spleen, central nervous system, gut, bone-marrow and in wound healing and tumour biology.

2. Results

2.1. Morphological study of mesoscopic placental tissue

2.1.1. Comparative analysis of tissue preparation for X-ray micro-tomography of complex soft tissues

The preparation of placental specimens for synchrotron micro-CT requires careful fixation, perfusion, staining and dehydration/embedding (electronic supplementary material, figure S1). Here, we apply and qualitatively evaluate various specimen preparation methods to successfully image the complex architecture of the human placenta (figure 1). Tissue zinc-based fixative Z7 applied to all specimens provides tissue contrast when in-line phase contrast synchrotron imaging is performed (electronic supplementary material, figure S2). Specimen 2 (electronic supplementary material, figure S2A, D, G–J), fresh-frozen by plunging in liquid nitrogen, preserves the physiological structures.

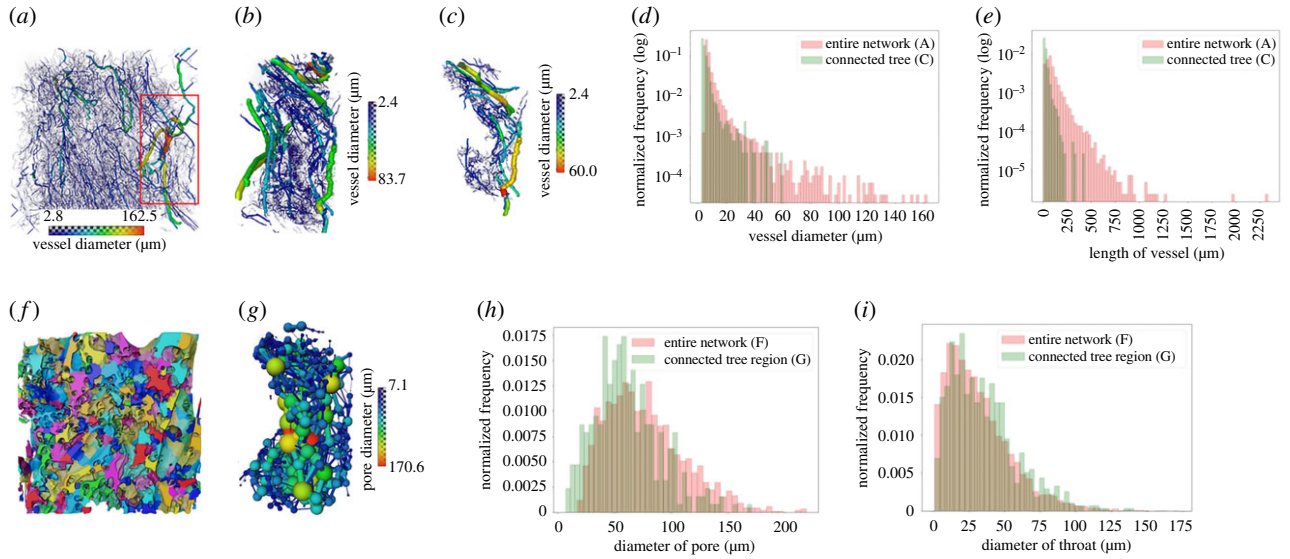

Figure 2. Three-dimensional analysis of the structure of the fetal vascular network and maternal porous space (Specimen 1, normal placenta at term). (*a,b*) Skeletonized vascular structure from the entire tissue volume and from a small cropped region (the red box in *a*). (*c*) A single connected vascular tree in the cropped region shown in (*b*). (*d,e*) Distributions of vessel diameter and length of blood vessels from the entire fetal vascular network and the connected vascular tree shown in (*a*) and (*c*), respectively. (*f*) Porous regions in the central tissue region (approx. 1.8 mm^3). The colours represent different porous regions but are not related to the sizes of the pores. (*g*) Ball and stick model to represent pores and throats in the cropped region as in (*c*). (*h,i*) Distributions of diameters of porous regions and connecting throats in the central tissue region and the region that encompasses the single connected tree in (*c*).

Placental architectures, including a well-resolved syncytiotrophoblast, blood vessels, capillaries, red blood cells and stroma, can be differentiated in the 2D cross-sectional and 3D rendered images. The syncytiotrophoblast appears as a thin (approx. 3 µm) envelope around an intermediate villous (figure 2*g*). It is also possible to observe aggregated nuclei within a syncytial knot (figure 2*g–j*). In Specimen 3 (electronic supplementary material, figure S2B, E, K,L) which was fixed with tissue fixative Zinc-7, ethanol dehydrated and wax-embedded, blood vessels, stroma and separately resolved microvillous and syncytiotrophoblasts are visible. Rendered 3D volumes in electronic supplementary material, figure S2 K, seem to show the presence of pores/open channels on the syncytiotrophoblast [12] which envelopes an intermediate villous circled in electronic supplementary material, figure S2 L. From here, a machine-learning algorithm (U-Net) can be applied to segment and quantify the intervillous space (IVS) but not the vascular network or the stroma. Additional staining with 1% phosphotungstic acid (PTA) solution can further enhance the contrast for stroma (electronic supplementary material, figure S2F; Specimen 4) making it segmentable. PTA solution has low viscosity and so infiltrates into the IVS but takes several days (3 days for an 8 mm^3 sample) to provide good contrast and signal to noise.

In order to confidently segment the complex 3D vascular network, resin infiltration casting via the fetal villi network is required to give sufficient contrast and phase differences. Specimens 1 (electronic supplementary material, figure S2C) and 3 (electronic supplementary material, figure S2B, E, K,L) were Zinc-7 fixed and perfused via the fetal side with casting resins (Batson's and Yasuaki's resins for Specimens 1 and 3, respectively), then ethanol dehydrated and wax-embedded. Batson's contrast agent penetrates deeply into the feto-placental circulation (electronic supplementary material, figure S2C) but shrinks inside larger vessels and possibly over-inflates smaller vessels, due to the high exertion force needed to infuse the resin via the fetal arterial cannula. Yasuaki's resin is less viscous and highly X-ray attenuating than Batson's and shrinks less, thereby likely better preserving vessel diameters. Both agents give good contrast to highlight the fetal lumen (electronic supplementary material, figure S2B,C). The viscosities of both Batson's and Yasuaki's reagents make them unfavourable for infusion into the IVS since filling is incomplete. The extent of tissue processing influences final architecture. Ethanol dehydration and wax embedding (Specimens 3 and 4) may introduce tissue deformation, in particular the villous trophoblast appears to delaminate from the villi stroma (electronic supplementary material, figure S2B,E). Tissue deformation occurred to much less extent with CP-dried specimens (Specimen 1; electronic supplementary material, figure S2C). While cryo-freezing seems to have caused syncytiotrophoblast shedding to occur, overall, it has preserved the morphology of specimens more than the other methods. However, synchrotron micro-CT imaging of cryo-frozen specimens requires a cryo-stream or cold stage to maintain the specimen at cryo-condition during scanning. Electronic supplementary material, figure S1A, provides a summary of various sample processing conditions tested here and a flow chart (electronic supplementary material, figure S1B) that recommends appropriate processing pipelines to resolve the multi-scale structures in the placenta.

2.1.2. Characterization of feto-placental vascular network in three dimensions

Feto-placental vascular network and porous materno-placental tissue domain were quantified in three dimensions for Specimen 1 (normal) and Specimen 2 (pregnancy with fetal growth restriction, FGR). The scanned 9 mm^3 cubed samples generated approximately 8 mm^3 of digital 3D data. The entire volume (14.2 billion voxels) was segmented and analysed to identify placental tissue architecture across multiple scales (figure 1; electronic supplementary material, video S1). A disambiguated 3D rendering (figure 1*b*) from the entire volume

of tissue demonstrated the sample tissue volume and three-dimensionality achieved with the technique, while the detail in the terminal capillary loops and surrounding villous tissue (figure 1*g*) demonstrated the resolution. Two separate 2D U-Nets (electronic supplementary material, figure S1) were used alongside expert-generated training data (electronic supplementary material, figure S3) to fully segment the feto-placental vascular network and the maternal and fetal blood volumes (figure 1*c*,*e*–*g*).

Once the complex tissue was segmented, multiple data analysis pipelines and simulations could be run, across the imaging scales. Figure 2 displays the skeletonized vascular structure from the entire tissue dataset (figure 2*a*), a small cropped region (figure 2*b*) and a single connected tree (figure 2*c*). The median (interquartile range; IQR) diameter of blood vessels in fixed tissue is 6.8 (IQR: 6.2–8.6) µm for the entire network and 4.4 (IQR: 3.4–6.0) µm for a single connected tree (figure 2*d*), while the length of blood vessels is 73.8 (IQR: 47.4–115.6) µm for the entire network and 21.2 (IQR: 13.6–34.1) µm for a single connected tree (figure 2*e*). Tortuosity of the blood vessels is 1.2 (IQR: 1.1–1.4) for the entire network (electronic supplementary material, figure S4) and 1.2 (IQR: 1.1–1.3) for a single connected tree. A limitation in the current analysis is that skeletonization and quantification of blood vessels for the entire network (figure 2*a*) was carried out on down-sampled image data due to computational limitations. Therefore, the measurements from the entire vascular network are likely to be less accurate in comparison to those from the single connected tree, where the full resolution data were used.

2.2. Characterization of the porous materno-placental tissue domain in three dimensions

To characterize the maternal blood porous space, the centre region of the scan, approximately 1.8 mm^3 from the entire dataset (see electronic supplementary material, figure S3A) and the porous space that encompasses the single connected tree (from figure 2*c*) were used. The median diameter of pores is 72.2 (IQR: 50.6–97.2) µm for the central region and 57.6 (IQR: 40.6–77.8) µm for the single tree region. The diameter of the throat (a throat is a region that connects two individual pores) is 27.0 (IQR: 14.4–43.6) µm for the central region and 31.0 (IQR: 16.8–47.0) µm for the single tree region. The distributions of the diameter of porous regions and connecting throats of both the central region and the region that surrounds the single connected tree (both from Specimen 1) are shown in figure 2*h*,*i*. The median and interquartile ranges of the diameter of the pore and throat, length of the throat and number of connected pores were also analysed for both Specimens 1 and 2, and the results are presented in electronic supplementary material, figure S5. These analyses were performed on central tissue regions only.

The flow tortuosity of porous regions was plotted with different minimal lengths. The smallest minimal length employed here (85 µm) is bigger than the mean diameter of a pore (approx. 80 µm) since the blood flow inside a single pore is considered straight. Electronic supplementary material, figure S6G, shows that the porous tortuosity falls between 1 and 3 in both Specimens 1 and 2.

2.3. Mesoscopic flow analysis in the human placenta

Using Specimen 1, the maternal flow velocity in the IVS was simulated for a fixed pressure gradient applied in three principal directions (figure 3; electronic supplementary material, video S2). The relationship between fetal tissue (figure 3*a*(i)) and maternal flow (figure 3*a*(ii)) in velocity map and streamlines, respectively, and the inter-relationship between maternal flow streamlines (figure 3*b*) and fetal vascular network (figure 3*c*) were visualized. The distributions of flow velocities (figure 3*d*) were in the range 0–1670 (mean: 8) µm s^{-1} in the x-direction, 0–1670 (mean: 10) µm s^{-1} in the y-direction and 0–1660 (mean: 7) µm s^{-1} in the z-direction.

Despite the approximately $1:2:1$ ($x:y:z$) aspect ratio of the studied porous domain, the flow resistance in the y-direction was found to be approximately twice as small as in the x- and z-directions, with the corresponding diagonal components of the empirical hydraulic permeability tensor approximately (1.5, 3.4, 2.0) μm^2, indicating a relatively strong flow anisotropy of the IVS.

The connectivity of the IVS domain was also explored as a function of the minimal pore–throat diameter needed to connect a random central pore to the periphery of the domain (electronic supplementary material, figure S6A–F). Such critical diameter was found to be just about 25% of the pore size, pointing to a highly connected IVS that facilitates flow-limited transport at the tissue mesoscale of approximately 1 mm (see electronic supplementary material, S8 for more details).

2.4. Uncertainty quantification and scale-dependence of morphological metrics

Placental tissue area fraction fluctuates across the 3D volume in both specimens. Based on the central tissue region (approx. 1.8 mm^3), the area fraction of Specimen 1 ranges from 0.54 to 0.73 (mean: 0.64) and that of Specimen 2 ranges from 0.58 to 0.71 (mean: 0.65; figure 4*a*; electronic supplementary material, figure S7A,B). The tissue volume fractions for Specimens 1 and 2 are 0.64 and 0.65, respectively. Figure 4*b* shows how the standard deviation of the volume fraction decreases with increasing region of interest (ROI) size (see also electronic supplementary material, figure S7C). The scale-dependent error in fetal tissue volume fraction, specific surface area (figure 4*c*) and the 2-point correlation function versus distance for both specimens (figure 4*d*) are also presented.

Figure 4*c* illustrates that the relative magnitude of fluctuations in both the tissue volume fraction and specific surface area fall approximately inversely proportional to the square root of the ROI volume ($\sigma/\mu \sim {V_{\mathrm{ROI}}}^{-1/2}$) for the sufficiently large ROI size (compared to the characteristic lengthscale $\lambda \sim 200$ µm; figure 4*d* and table 1). This is in agreement with theoretical predictions for a generic porous medium (see electronic supplementary material, S9 for more details). Thus, to reduce the estimation error in morphological metrics by a factor of 2, a fourfold increase in the ROI volume is required. For smaller ROI volumes (i.e. when the ROI size is less than *ca* 200 µm), the morphometric fluctuations are even more sensitive to the measurement scale.

Three-dimensional morphometrics were also compared to the estimates based on 2D 'virtual' stereology (electronic supplementary material, figure S8) on the same dataset to

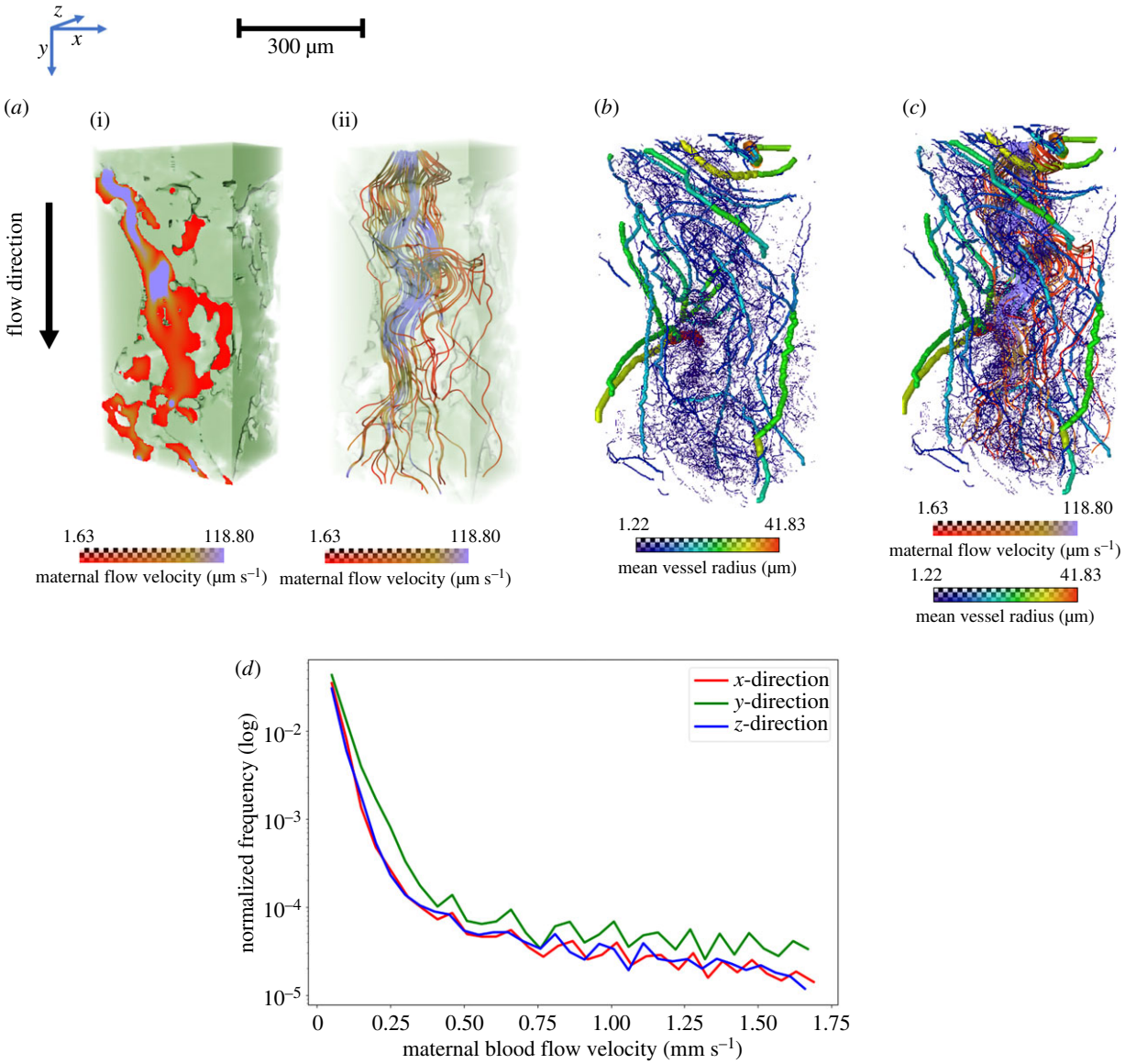

Figure 3. Flow simulations across maternal IVS to visualize the inter-relationship between maternal blood flow and fetal vascular flow (Specimen 1, normal placenta at term). (*a*) The maternal (i) flow velocity map and (ii) flow streamlines in the IVS. (*b*,*c*) The inter-relationship of maternal flow streamlines and fetal blood vascular network. (*d*) Line graphs comparing the maternal blood flow velocity distributions in three different directions with a fixed pressure gradient. The *x*-axis of the graph shows maternal blood flow velocity and *y*-axis shows the normalized frequency in logarithmic values.

cross-validate the estimated tissue volume fractions and specific surface areas between these two approaches. Table 1 reports the villous tissue volume fraction and specific surface area for Specimen 2 estimated by traditional 2D stereology and 3D morphological analysis. Comparison to the direct 3D estimates (table 1) shows good agreement for the volume fraction but an up to 40% relative difference for the specific surface area.

3. Discussion

In this study, we present a novel approach to quantitatively characterize the 3D structure of complex mesoscale tissues using the human placenta as a model. We demonstrate how up to four orders of magnitude can be bridged in a single imaging dataset using synchrotron X-ray micro-tomography, and propose an optimized pipeline for tissue sample processing and image segmentation to robustly evaluate morphological data of complex vascular systems. To our knowledge, this is the first study to characterize the maternal placental IVS porous region and to demonstrate the inter-relationship between maternal blood flow and fetal vascular network. Finally, we compare traditional stereological approaches with direct 3D structural analysis and quantify the scale-dependent fluctuations in common morphological metrics. The developed framework helps to identify a minimal characteristic size for heterogeneous placental and other complex soft tissues and provides the tools to control the associated uncertainties for robust and scalable predictions.

The placental specimens in this study were prepared using different tissue processing techniques (critical point (CP)-drying, fresh-frozen, wax embedding) and perfused with different contrast agents (Batson's and Yasuaki's; electronic supplementary material, table S1). CP-dried and wax-embedded specimens showed more deformation and shrinkage of villous tissue in comparison to fresh-frozen specimens that maintained the tissue at near-native anatomical condition. Among the three processing techniques,

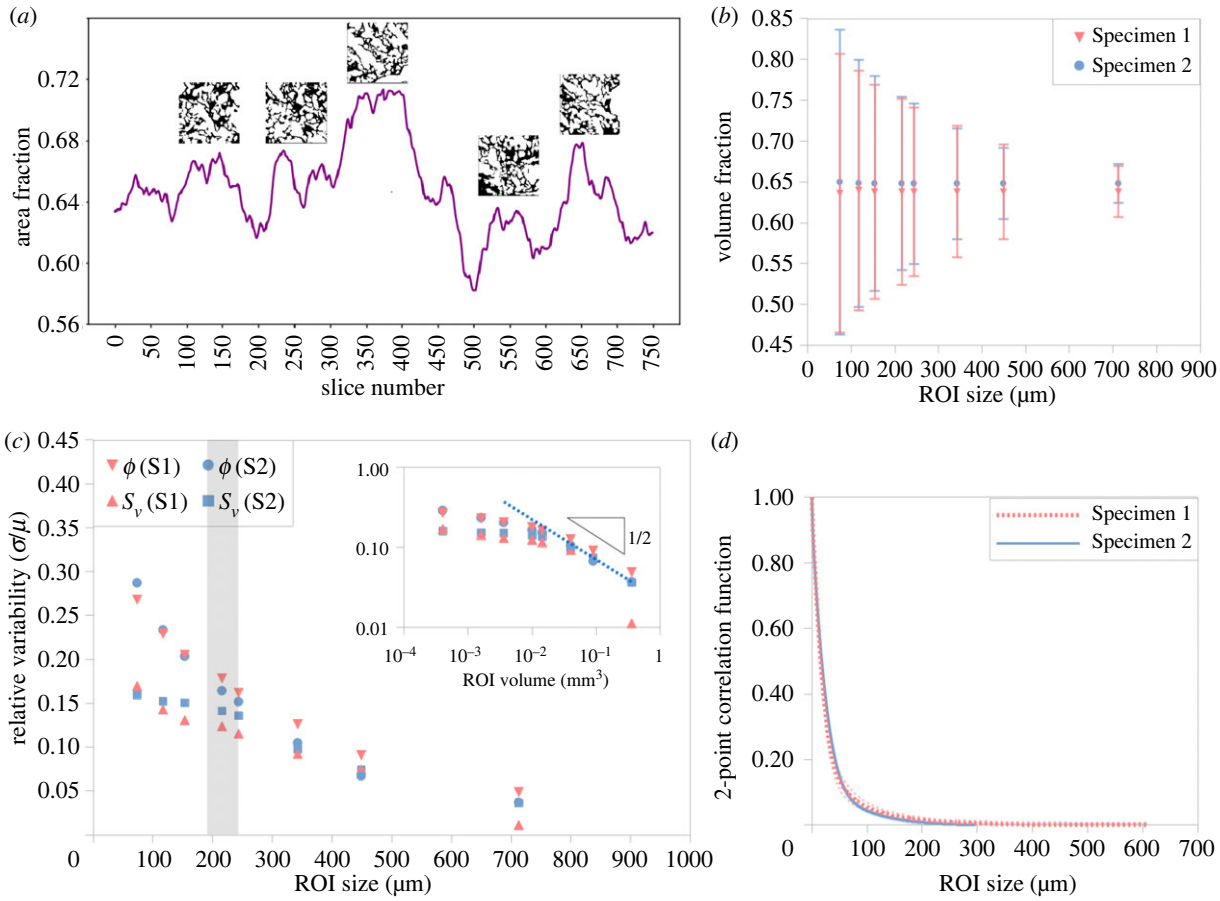

Figure 4. Uncertainty quantification and scale-dependence of morphological metrics (Specimens 1 and 2). (*a*) Fluctuations of placental villous tissue area fraction in Specimen 2 for the ROI with a volume of approximately $1.22 \times 1.22 \times 1.22$ mm^3 (insets illustrate selected slices). (*b*) Volume fraction fluctuations (mean ± s.d.) versus effective ROI size. (*c*) Scale-dependence of a relative error in the tissue volume fraction (ϕ) and specific surface area (S_v) estimates; the inset compares to the theoretical prediction of ~(ROI volume)$^{1/2}$ on a logarithmic scale (see electronic supplementary material, S9). (*d*) Radial two-point autocorrelation function (mean; s.d. is shown with shaded lines); the corresponding approximate transition range to uncorrelated mesoscale (mean autocorrelation $\lesssim$1%) is shown as a grey stripe in (*c*).

CP-dried specimens displayed the best image contrast between fetal tissue and maternal IVS (electronic supplementary material, figure S2). Yasuaki's gave a superior contrast of the fetal vascular network than Batson's, meaning Yasuaki's-perfused specimens could be easily segmented with contrast-based image segmentation methods while Batson's-perfused specimens require more complex segmentation strategies. However, one drawback with Yasuaki's resin was lower perfusion efficiency which manifests as smaller arterioles and venules in the terminal capillaries. Sample processing must be considered in the light of both the preservation of the region of interest, but also the downstream data analysis and segmentation strategy (electronic supplementary material, figure S1A). In an ideal case (electronic supplementary material, figure S1B), specimens would immediately be Z7 fixed, fetal network infiltrated with a resin, paraformaldehyde (PFA) fixed, and then cryo-frozen and micro-CT imaged under cryo-conditions. If a cryo-stage is not available then specimens should be ethanol dehydrated and CP-dried before imaging under ambient conditions. In order to segment the various structures, a machine-learning algorithm (U-Net) should be employed. This proposed sample preparation and imaging pipeline would be applicable to other vascular-rich organs [13–15].

In recent years, automatic or semi-automatic segmentation methods using deep learning algorithms have become popular in the vascular biology [16] and placental biology fields [17]. Convolution neural networks (e.g. U-Net) have been successfully applied in segmenting various vascular systems including retina [18,19], brain [20], whole placental volume [21] and larger placental vessels [22]. Here for the first time, we apply a U-Net towards multi-domain

Table 1. Comparison of 2D- and 3D-based placental tissue morphometrics (Specimen 2; see electronic supplementary material, figures S7 and S8 for more details). n.a. indicates the technique is not applicable.

structural metric	2D stereology (mean ± s.d.)	3D micro-CT
volume fraction[a]	0.67 ± 0.04	0.65
slice-averaged area fraction[b]	n.a.	0.65 ± 0.03
specific surface area (S_v, μm^{-1})[c]	0.028 ± 0.006 (range: 0.017–0.037)	0.045
characteristic correlation lengthscale (λ, μm)[d]	n.a.	≈200

[a]Based on the 2D ROI area of approximately 1.46×1.46 mm^2.
[b]Based on the central ROI volume of approximately $1.22 \times 1.22 \times 1.22$ mm^3.
[c]Based on the ROI area of approximately 0.44×0.44 mm^2.
[d]The distance at which the mean of normalized autocorrelation function falls below 1%.

segmentation of the intricate fetal vascular network and maternal porous space, including terminal capillary loops where vessel diameters are smaller than 50 µm. The semi-automatic algorithm used here requires a minimal amount of training data (approx. 1% of entire volume). The most striking aspect of the U-Net segmentation is the detection of the smallest terminal capillaries, with diameters of the fixed tissue as small as approximately 2.5 µm (IQR: 6.2–8.6). These tiny terminal capillaries are exceedingly difficult to segment manually, so their presence in the U-Net segmentation provides a less time-consuming and more consistent method for their inclusion in analyses.

The U-Net predictions were assessed by dice score coefficient, a commonly used voxel-based validation metric for image segmentation algorithms [23]. Using the dice score, comparisons between multiple manual expert segmentations of complex, biological components have varied between approximately 0.27 and approximately 0.69 [24]. When comparing the U-Net segmentations to expert manual validation segmentations, the dice scores for vascular and tissue regions are 0.8 and 0.9, respectively (electronic supplementary material, figure S9). There are, however, some artefacts present in the U-Net segmentation (mislabelling of maternal porous region as fetal tissue) that could lead to overestimation of the surface area of fetal tissue. In addition, the current U-Net model was not able to generalize across datasets, instead requiring manual training data from each individual dataset. This may be due to the variation in specimen processing and imaging, which manifested significantly different appearances in the final datasets.

Understanding the structural development of the placenta is critical since the common pregnancy disorders FGR and pre-eclampsia are associated with impaired development of the placental vascular network [25,26]. The human placenta is haemochorial and possesses a dual blood supply; maternal and fetal circulations are separated, but work collaboratively as a multi-villous exchange system [27]. Defects in either supply could impair nutrient and gaseous exchange. Here, we have quantified the continuous fetal vascular networks from an approximately 8 mm^3 placental tissue block capturing the transition from the micro- to mesoscale, with the size range of blood vessels and intervillous pores of the order of 10–1000 µm (figure 2). In order to appreciate the spatial inter-relationship between these two circulations, we have visualized the maternal flow intertwined with the fetal vascular network (figure 3*c*). We simulated maternal blood flow in a large portion of the segmented intervillous pore space for a fixed pressure gradient of approximately 10 Pa mm^{-1} within placental tissue [28,29]. The predicted flow had an exponential distribution of velocities, typical for a random porous medium [30], with the range of approximately 0–2 mm s^{-1}. This is consistent with previous magnetic resonance imaging *in vivo* estimations that reported regions of slow (less than 0.5 mm s^{-1}) and fast (greater than 1 mm s^{-1}) blood flow [31]. Furthermore, our results suggest a new hypothesis that local IVS pore sizes influence nutrient and gaseous exchange efficacy. Future studies are needed to identify whether IVS porosity spatially correlates with the calibres and orientation of associated villous microvessels, and to determine the extent of maternal–fetal placental flow matching. The impact of villous tissue compliance on flow distribution in the IVS, particularly in the proximity of decidual arterial inflows, also warrants further investigation.

With the intention of understanding the normal physiological blood flow and deviations occurring in diseased pregnancies, numerous mathematical and computational models have been developed and attempt to replicate the utero-placental circulations [11,32–34]. A particular challenge is the geometric complexity of intervillous maternal porous regions which are difficult to characterize [33]; therefore, there is a lack of knowledge on placental porous structure. Porosity within human tissues has been extensively investigated in bone and other soft tissues (e.g. adipose tissue) from the perspective of tissue engineering [35–38]. Nonetheless, the placental maternal IVS porous medium has been less well studied. Here, we have quantified the size of porous regions, the connecting throats between individual pores and the length of connecting throats. Moreover, we report the number of coordination for individual pores, and also visually examine the connectivity by thresholding the size of connected regions (electronic supplementary material, figure S6). Both qualitative and quantitative analyses suggest that the maternal porous space is highly connected and there is no unconnected, isolated porous region. The minimal diameter of the throat is 0.86 µm (IQR: 14.4–43.6), in line with the average thickness of a human red blood cell (0.8–1 µm), indicating blood flow could occur throughout the porous medium with some impedance [39]. However, the resistance to IVS flow would vary depending on the length and diameter of connecting throats/pores, suggesting a potential explanation for the heterogeneous maternal flow velocity reported in [29] and also in our flow simulations.

Contrast imaging and mesoscopic flow analysis reported here could readily be applied to other organs where it is challenging to understand structure–function relationships when a fluid circulates around epithelia or where flow is not confined to a vascularized system. This type of anatomy can be found in the intestine and the central canal of the spine. In the gut, the uptake of nutrients and therapeutic compounds occurs from the crypts of the jejunum lumen, passing into the systemic circulation having traversed associated villi. The crypt lumen has been observed to become vacuolated following chemotherapy, altering the porosity, which is hypothesized to affect the efficacy of nutrient and therapeutic uptake [40]. In a second example, the motile cilia of the spinal cord central column and brain generate an efficiency of cerebrospinal fluid flow that is sensed and regulates structural modelling of the shape of an organism during embryonic development [41]. Thus, the workflow we have developed could provide anatomical insights on tissue structure and function in homeostasis and pathology.

It is important to note that the pore diameters measured here could be influenced by the flow and the hydrostatic pressure within the IVS during perfusion fixing, compared to non-perfusion fixed tissue, where villous and IVS deflation could occur [42]. Following partum, the placenta collapses and loses a significant volume of maternal blood from the IVS. However, a more physiological pressure and flow within the IVS *in vivo* can be recapitulated during *ex vivo* dual perfusion of the human placenta, yielding a more normal spatial arrangement of villi compared to the arrangement produced by the direct immersion fixing of deflated placental material. Consequently, most historic stereological analyses have likely underestimated the volume fractions of the IVS in this tissue [42]. In turn, this will have led to an under-representation of pore size diameter and connectivity

characteristics. However, potential confounders of the *ex vivo* perfusion model relate to an artificial rheology, created by a blood-free environment, with some compromise in viscosity linked to altered shear stress within the two circulatory systems. One unresolved question is how to determine the tissue sample size required to accurately obtain statistically representative data. This is particularly true for placental tissue due to its inherent heterogeneous nature. While it is true that the larger the tissue section, the more information one can retrieve, using a large-sized sample comes with technical and economic burdens. Therefore, systematically characterizing the minimal tissue size that could provide adequate information with the least error is advantageous. Using uncertainty quantification and scale-dependence of morphological metrics applied to a variety of placental tissue samples, we identified a transition from microscopic fluctuations to tissue-scale properties at the mesoscale of approximately 200 µm (table 1). Thus, the smallest ROI volume required, without failing to comprehend the heterogeneous nature of the finest features of exchange villi in placental tissue, is of the order of magnitude of 0.1 mm^3 (figure 4). Although this smallest cut-off point might vary in other tissues with different geometric properties (e.g. larger blood vessels), the generic scale-dependence of the magnitude of 3D morphometric fluctuations (inversely proportional to the square root of the ROI volume, extending the results of [43]) is shown to be sufficiently universal for a wide class of porous media found in biological solute and gas exchangers. Future work is needed to further refine and extend the developed framework to placental pathologies and to other organs.

In conclusion, this paper offers both a novel approach and a validated workflow for massively multi-scale characterization of soft tissues with complex vascular networks. In addition, several detailed morphology and functional characteristics of our chosen model tissue, placenta, have been analysed in three dimensions. In future, these methods could be used to explore underlying causes of disease and inform potential future treatments.

This approach was enabled by a combination of innovative sample preparation, advanced synchrotron-based imaging and state-of-the-art segmentation algorithms that bridge the gap of previously disconnected characterization strategies using traditional X-ray tomography and angiography (cf. figure 1*a*), light microscopy (cf. figure 1*b*) and confocal or electron microscopy (cf. figure 1*f*). In the placental research arena, the data generated here represent, for the first time, a multi-scale approach applied to characterize the architecture of both maternal and fetal domains by synchrotron micro-CT. Additionally, the recommendations provided for future researchers should allow translating the workflow to quantify structures in other complex, soft tissues.

4. Methods

4.1. Specimen collection and preparation

4.1.1. *Ex vivo* placental perfusion and preparation of tissue blocks

Ex vivo dual perfusion of human placental cotyledons was conducted as previously described [42] from two pregnancies complicated by FGR and two from uncomplicated pregnancies (see electronic supplementary material, table S1). Briefly, placentas were collected within 30 min of delivery and the chorionic plate artery and vein corresponding to an intact cotyledon were each cannulated. A suitable cotyledon was selected on the basis of intactness following delivery. Peripheral cotyledons were not excluded. Fetal-side perfusion was commenced in an open circuit at 6 ml min^{-1} with a modified Earle's bicarbonate buffer, gassed with 5% CO_2/bal. N_2. Following a quality control check at $T = 5$ min that fetal-side venous outflow was greater than or equal to 75% of fetal-side inflow, the maternal-side perfusion was commenced in open circuit at 14 ml min^{-1} with the same buffer, gassed with 21% O_2/5% CO_2/bal. N_2, via a single glass cannula (i.d. = 2 mm) held 5 mm below the decidua surface. The maternal cannula was inserted at the centre of a placental cotyledon. For the tissue mass of *ca* 30–40 g, this typically represented a random location of the insertion with respect to several villous trees within a cotyledon, below the decidual surface. The cotyledons continued to be perfused in open circuit for three hours prior to perfusion fixation from the maternal surface with Zinc 7 fixative [44] for 15 min. Various contrast reagents were infused into the fetal or maternal circulatory compartments (electronic supplementary material, table S1).

Colloidal dispersion of NiAl layered double hydroxide (LDH) 'Yasuaki' resin was prepared following our previous report [45]. Briefly, $NiCl_2{\cdot}6H_2O$ and $AlCl_3{\cdot}6H_2O$ were dissolved in a mixture of EtOH and ultra-pure water followed by the addition of acetylacetone (acac). To this mixture, propylene oxide was added as an alkalization agent [46] and the container was sealed and kept at a room temperature (RT ~ 20°C). The obtained suspension was kept in a freezer (−20°C) and then dried under a vacuumed condition (<10 Pa), yielding dried NiAl LDH nanoparticles. To make up 5 ml of resin, the powdery NiAl LDH (1.0 g) was dispersed in ethanol (EtOH; 2.5 ml), and then methyltriethoxysilane (2.0 ml) and tetraethyl orthosilicate (0.5 ml) were added to this mixture. Then, H_2O (0.7 ml) was added just before perfusion to initiate the gelation reaction. The procedures were performed under stirring at RT. This resin was applied immediately after fixing the lobule *in situ* within the perfusion cabinet, ahead of any other contrast reagents that might have been used.

On occasions, a Batson's resin from the 'Batson's no. 17 Anatomical Corrosion Kit' (Polysciences, Inc., Europe) was applied to the fetal circulation following perfusion. The liquid resin was prepared as a 20 ml base solution, 2.4 ml of catalyst and one drop of promoter; and manually injected via the chorionic plate arterial cannula until emergent at the chorionic plate vein cannula. Both cannulae were clamped and the whole lobule was allowed to polymerize overnight on iced water, within a sealed plastic bag.

The postperfusion fixed and post-contrast-infused cotyledon was excised from the non-perfused tissue and a 5 mm vertical slice of the cotyledon, adjacent to the inflow locus of the maternal cannula, was dissected from the cotyledon and fixed in a PFA fixative overnight to stiffen and further preserve the tissue. In all cases, following PFA diffusion fixing, 5 mm sized cubes were dissected from the vertical tissue sections and stored in sterile PBS. In some cases, the small blocks were infused with a further contrast agent, PTA, for several days or hours. In other cases, the cubes underwent CP-drying using an E3100 Critical Point Dryer (Quorum, UK), following the manufacturer's instructions, and dipped into liquid nitrogen to freeze fracture a 3×3 mm^2 cross-sectional sample for imaging, or prior to wax embedding.

The methods for processing whole-organ vascular casts (figure 1*a*) were as previously described [5].

4.1.2. Three-dimensional tomographic imaging

At the Diamond Light Source (DLS) facility (Harwell, UK; Manchester Imaging Branchline, I13–2), in-line high-resolution synchrotron-sourced phase contrast micro-computed X-ray

tomography was used to generate images, following various methodologies to optimize image quality and feature extraction [47,48]. Briefly, micro-computed tomography employed filtered (1.3 mm pyrolytic graphite and 3.2 mm Al filters) polychromatic X-ray beams with energy in the range of 8–30 keV to probe the samples. Transmitted X-rays produce visible light on striking a scintillator (500 µm thick $CdWO_4$) positioned between 60 and 100 mm away, in-line with the sample. The light was then magnified with various objectives and imaged on a sCMOS (2560 × 2160 px) detector (pco.edge 5.5; PCO AG, Germany). An optical magnification of 8× was employed resulting in an effective isotropic pixel size of 0.81 µm. In total, 3001–4001 X-ray projections were recorded over 0–180° rotation using exposure times between 80 and 200 ms. Projections were reconstructed into 3D datasets using a filtered back projection algorithm [49] incorporating dark- and flat-field correction, ring artefact suppression and lens-blurring [50,51].

Samples ($3 \times 3 \times 3$ mm^3 cubes) were prepared following various methodologies (see above and electronic supplementary material, table S1) to optimize image quality and feature extraction. Specimen 1 was ethanol dehydrated then CP-dried and imaged at RT (60 mm S-D distance, 3001 projections, 0.08 s exposure). Specimen 2 was plunge frozen into liquid nitrogen and imaged (60 mm S-D distance, 4001 projections, 0.15 s exposures) while maintaining a sample temperature of −20°C using a cold stage [52]. Specimen 3 was ethanol dehydrated then wax-embedded and imaged at RT (100 mm S-D distance, 4001 projections, 0.2 s exposure). Specimen 4 was PTA stained, ethanol dehydrated then wax-embedded and imaged at RT (10 mm S-D distance, 4001 projections, 0.2 s exposure).

4.2. Segmentation

'Ground-truth' training data for Specimen 1 were created using SuRVoS (Super Region Volume Segmentation Workbench) which applies a supervoxel segmentation strategy as described in [53]. A 256 × 256 × 256 px (0.21 × 0.21 × 0.21 mm) region of the full resolution volume was segmented for the feto-placental vascular network and a 384 × 384 × 384 px (0.31 × 0.31 × 0.31 mm) region was segmented into the maternal and fetal blood volumes. These segmented regions along with the corresponding image data were then used to train two separate 2D U-Net models for binary segmentation [54]. All aspects of model construction, training and data prediction were done using the fastai deep learning Python library [55]. The U-Net model architecture used a ResNet34 [56] encoder that accepts images of size 256 × 256 px and that had been pre-trained on the ImageNet dataset [57]. For model training, both the segmented label volumes and the corresponding data volumes were sliced into 2D parallel to the *xy*, *xz* and *yz* planes. For each model, a randomized dataset was created from the pool of images with an 80%/20% split between training and validation image sets. The default fastai image transformations and augmentations were used. Model training was carried out using binary cross-entropy as the loss function and evaluated using the Intersection over Union (IoU/Jaccard) score as the metric on the validation set. For the vascular network data, training was carried out for 10 epochs giving a final IoU score of 0.93 on the validation set, the loss for the training set was 0.056 and the corresponding loss for the validation set was 0.052. For the maternal/fetal blood volumes, training was carried out for 15 epochs, giving a final IoU score of 0.93 on the validation set, the loss for the training set was 0.099 and the corresponding loss for the validation set was 0.097.

To overcome the issues of using a 2D network to predict 3D segmentation, a data-averaging approach was developed. To generate the vascular network and maternal/fetal blood volume segmentations for the full 2520 × 2520 × 2120 px (2.05 × 2.05 × 1.72 mm) data, the image data volume was sliced into three stacks of 2D images parallel to the *xy*, *xz* and *yz* planes. The corresponding segmentation for each of these image stacks was predicted before being recombined back into a 3D dataset, thereby producing three separate segmented volumes. The image data volume was then rotated by 90° around the fourfold symmetry axis running perpendicular to the *xy* plane and the entire slicing and prediction process was repeated again. After four cycles of this process, the resulting 12 segmented volumes were summed and a final segmentation produced by applying a threshold to the data where there was agreement between six and more of the predictions in the case of the maternal/fetal blood volumes and between nine and more of the predictions in the case of the blood vessels.

To segment the fetal tissue components from Specimen 2, the central region of the full resolution dataset (2520 × 2520 × 2120 px = 2.05 × 2.05 × 1.72 mm) was cropped to obtain a volume of 1500 × 1500 × 1500 px (1.22 × 1.22 × 1.22 mm) (see electronic supplementary material, figure S3A), which was then down-sampled to obtain a volume of 750 × 750 × 750 px. This down-sampled, cropped volume was then split into eight subvolumes, each of which were manually segmented using SuRVoS (electronic supplementary material, figure S3B–D).

Segmentation and analysis along with U-Net training and prediction were carried out on a High-Performance Computing Cluster node. The node had two Intel® Xeon® Gold 6242R processors each with 20 cores running at 3.1 GHz, and 768 GiB of system memory. The GPU used was an NVIDIA Tesla V100 with 32 GB of available memory.

4.3. Validation of semi-automated segmentation by U-Net

To validate the U-Net prediction of fetal vascular network in Specimen 1, two different regions of 384 × 384 × 384 px (0.31 × 0.31 × 0.31 mm), which were located away from the original training data, were randomly chosen and SuRVoS-segmented manually. The similarities between the SuRVoS segmentations and the U-Net predictions (electronic supplementary material, figure S9A,B) were compared using the Sørensen dice score = $2|M \cap U|/(|M| + |U|)$, which compares the area of the overlap ($M \cap U$) to the average area of the manually segmented (M) and U-Net-predicted (U) regions, respectively (estimated for each slice).

To validate the U-Net prediction of the fetal tissue component in Specimen 1, a similar strategy was used. Dice scores were again calculated between two SuRVoS-segmented validation regions (256 × 256 × 256 px; 0.21 × 0.21 × 0.21 mm) and the U-Net prediction (electronic supplementary material, figure S9C,D). The fetal tissue area fraction of individual slices was also compared between U-Net predictions and SuRVoS segmentations.

Electronic supplementary material, figure S9E,F, shows the dice scores for fetal vascular network segmentation and fetal tissue segmentation, respectively. The mean dice score for vascular validation Region no. 1 is 0.81 and that for vascular validation Region no. 2 is 0.88. Vascular Region no. 2 is likely to have a higher dice score because it contains fewer but larger vascular branches in comparison to vascular Region no. 1. The mean dice scores for tissue validation Region no. 1 and Region no. 2 are 0.97 and 0.96, respectively. A higher dice score in the tissue regions as opposed to the vascular regions is expected because the vascular network segmentation has more boundaries than the tissue segmentation, where most discrepancies between U-Net and SuRVoS segmentation occur. The area fraction comparison for tissue validation Region no. 1 and Region no. 2 (electronic supplementary material, figure S9G) confirms the consistent agreement between U-Net prediction and SuRVoS segmentation.

4.4. Computed tomography-based stereology

Following synchrotron imaging of a placental block, capturing $2520 \times 2520 \times 2120$ px^3 tissue (approx. 8 mm^3) at approximately 80 µm slice intervals with an image resolution of 0.8125 µm px^{-1}, systematic analysis of villous volume density and syncytiotrophoblast surface density was performed using a traditional stereology method, as described previously [58,59]. Every 100th image taken was imported into Image J software [60], providing 22 images in total (electronic supplementary material, figure S8A).

Within each image, a smaller 1800×1800 px^2 field of view (FOV) was generated systematically (electronic supplementary material, figure S8B). A grid of 11×11 dots was superimposed on the FOV. The number of grid points hitting the villi and IVS was scored and the volume density of each of these morphological features was assessed using

$$V_V = P_p/P_n,$$

where V_V is the volume fraction of the feature of interest, P_p is the number of points that hit features of interest and P_n is the total number of test points in the grid [59].

From each synchrotron image, a smaller 543×543 px^2 FOV was generated systematically (electronic supplementary material, figure S8C). A grid of 10×10 crosses (line length: 12 µm) was superimposed onto the FOV. In processing for surface density estimation, line intersects with the syncytiotrophoblast were scored ($N = 100$ intersects per image, $N = 22$ images). The horizontal lines were used as intercepts to estimate the specific surface area of syncytiotrophoblast $S_{V(\mathrm{syn})}$ within tested volume:

$$S_{V(\mathrm{syn})} = 2I_L,$$

where I_L is the intersection count fraction (the number of intersections with the villous boundary per unit length of test line) [61].

4.5. Three-dimensional morphological analysis

4.5.1. Structural analysis of fetal vascular network

The structure of the fetal vascular network (Specimen 1) was analysed using Avizo software 2020.1 (Thermo Fisher Scientific). Using the *Centreline tree* module which extracts the centre lines of labelled 3D image volume as described in [62], the vascular network was skeletonized from placental tissue from the entire dataset of approximately 8 mm^3 (figure 2*a*) and a small cropped region of approximately 0.2 mm^3 (figure 2*b*). The vascular branching structure (length, diameter and tortuosity) of the entire network and a single connected tree inside the small cropped region was analysed. Only vessels with a diameter greater than or equal to 3 px (2.4 µm) were included since the vessels smaller than this could not be resolved.

4.5.2. Maternal porous region analysis

To evaluate the size and connectivity of the porous region (maternal IVS), the *Separate objects* module (Avizo 2020.1) using a watershed method [63,64] was employed on the labelled 3D image volume to separate the porous regions (figure 2*f*). Afterwards, the *Pore Network Model* module (Avizo) [62–64] was applied to generate the spheres at separated porous regions. The centres of two spheres were connected by 'throat' (a throat is a region that connects two individual pores) (figure 2*g*).

In analysing the maternal porous region, the central placental tissue region of approximately 1.8 mm^3 (see electronic supplementary material, figure S3A) and the porous region that encompasses the single connected tree (from figure 2*c*) were used. Distributions of diameters of pores and throat, length of throat and number of pore coordination (how many pores are connected to an individual pore) were analysed to characterize the placental porous medium.

The tortuosity of porous regions was analysed using the *Flow tortuosity* module (Avizo) which computes the tortuosity based on the flow velocity vector field (the output of the *Absolute Permeability Experiment Simulation* module [62,63]). The flow velocity vector was calculated using a fixed pressure drop across the domain (see below for more details). Porous tortuosity was computed with various minimal lengths and compared between Specimens 1 and 2.

4.5.3. Simulation of maternal blood flow in the intervillous space

Maternal blood flow into the IVS was simulated using the *Absolute permeability experiment simulation* module (Avizo 2020.1) which solves Stokes flow in a segmented intervillous porous space geometry [62,63]. The simulation was performed on the small cropped region of approximately 0.2 mm^3 (as described above). However, the dataset was down-sampled (2×) as flow simulation on full resolution data would be computationally prohibitive. The simulations were done in three directions (x, y and z) across the tissue thickness of approximately 500 µm (x- and z-directions) and approximately 950 µm (y-direction). Three simulations were performed with a fixed pressure gradient across the three principal directions (pressure drop of 10 Pa in the y, or 5 Pa in the x- and z-directions, respectively, accounting for approximately 1 : 2 : 1 ($x : y : z$) aspect ratio; i.e. approximately 10 Pa mm^{-1} within tissue [28,29]). The other four domain boundaries (in the transverse to the applied gradient direction) were assumed impermeable in each simulation, and a no-slip flow condition was used at the fluid–solid interfaces. A constant blood viscosity of 0.003 Pa s was assumed. The calculated net flow rate was used to estimate the empirical hydraulic permeability in each principal direction from Darcy's Law [62].

4.5.4. Characterization of fetal tissue component

The area and volume fraction of segmented fetal tissue components from Specimens 1 and 2 were analysed using the *Volume fraction* module (Avizo 2020.1). The surface area of segmented fetal tissue components was analysed using the *Label analysis* module (Avizo) which calculates the surface area of labelled regions from 3D image volume. The area fraction was analysed for individual slices. Volume fraction and surface area were analysed using different ROI sizes. To obtain the ROI cubes at different sizes, the tissue cubes with various x and y length and fixed z thickness (243.75 µm) were cropped without overlapping. For those ROI sizes with more than 1000 ROI cubes, a systematic random sampling method (picking nth ROI cubes) was used in order to get 1000 random ROI cubes for statistical analysis. For those ROI sizes with fewer than 1000 cubes, all ROI cubes were included. The analysis was done for both Specimens 1 and 2 and performed on the central tissue region (as shown in electronic supplementary material, figure S3A).

4.6. Statistical handling

For the purposes of stereology, a systematic random sampling protocol was used, where every 100th image from a stack of 2120 images was analysed for volume fraction and specific surface area ($N = 22$ fields of view).

Ethics. All human placental tissues used in this study were acquired from term placentas delivered at St Mary's Hospital, Manchester, UK, with appropriate informed written consent and ethical approval (Tommy's Project REC 15/NW/0829).

Data accessibility. All data needed to evaluate the results and conclusions are present in the paper and/or the electronic supplementary material. The reconstructed micro-CT volumes (DLS ID 120077 and 13761), manual segmentations (DLS ID 120077) and predicted final segmentations (DLS ID 123861) are available on public repository EMPIAR (https://empiar.org/10562/ and https://empiar.org/10563). The training data for U-Net and trained U-Net models for segmenting

the maternal/fetal blood volumes and the blood vessels are openly available at http://doi.org/10.5281/zenodo.4249627. The associated computational codes can be accessed at https://github.com/DiamondLightSource/python-placental-imaging and https://github.com/DiamondLightSource/placental-segmentation-2dunet. The supplementary methods, results and data are provided in the electronic supplementary material.

Authors' contributions. W.M.T. performed 3D image segmentation, data analysis and simulations, created movies and wrote the manuscript. G.P. contributed to project design, data collection and data analysis, proposed optimized pipeline for specimen preparation and data segmentation and wrote the manuscript. G.N. and H.B. refined and performed the perfusion and specimen collection, processed tissue and prepared blocks for imaging, and performed stereological analysis. O.N.F.K. developed the U-Net segmentation algorithm and wrote the manuscript. M.B. supervised development of U-Net segmentation algorithm, data segmentation, data analysis and movie creation. Y.T. developed and manufactured Yasuaki's resin. R.M.L. and E.D.J. contributed to the interpretation of results and provided critical feedback to shape the research, and wrote the manuscript. P.B. conceived and designed the project, performed tissue sample collections, sample preparations and stereological analysis, contributed to the interpretation of the results, provided critical feedback, supervised the project and wrote the manuscript. M.D. supervised image segmentation, data analysis and simulations, contributed to the interpretation of the results, provided critical feedback, supervised the project and wrote the manuscript. I.L.C. conceived and designed the project, designed and performed the scale-dependence error analysis, contributed to the interpretation of the results, supervised the project and wrote the manuscript. All authors discussed the results and contributed to the writing of the manuscript.

Competing interests. We declare we have no competing interests.

Funding. This work was partially supported by the MRC (MR/N011538/1), EPSRC (EP/T008725/1), Wellcome Trust (212980/Z/18/Z) research grants. G.P. would like to acknowledge the EPSRC grant EP/M023877/1 and Great Britain Sasakawa Foundation for funding.

Acknowledgements. Imaging was performed on the Branchline I13-2 of the Diamond Light Source synchrotron in Oxfordshire, UK, on beamtimes MG23941 and MG22562. The authors would like to thank beamline scientists Dr Andrew Bodey and Dr Shashi Marathe and collaborators Dr Saurabh Shah and Prof Peter D. Lee (University College London) for providing access to the cold stage and assistance with setting up. We also thank Dr James Carr, Dr Tristan Lowe, Dr Kerstin Schirrmann, Ms Ruth Whelan-Jeans and Ms Saskia Port (University of Manchester) for their help with pre-synchrotron optimization of micro-CT protocols and image analysis.

References

1. Lewis RM, Pearson-Farr JE. 2020 Multiscale three-dimensional imaging of the placenta. *Placenta* **102**, 55–60. (doi: 10.1016/j.placenta.2020.01.016)
2. Leiser R, Kosanke G, Kaufmann P. 1991 Human placental vascularization. In *Placenta: basic research for clinical application* (ed. H Soma), pp. 32–45. Basel, Switzerland: Karger. (doi:10.1159/000420847)
3. Thunbo MØ, Sinding M, Korsager AS, Frøkjær JB, Østergaard LR, Petersen A, Overgaard C, Sørensen A. 2018 Postpartum computed tomography angiography of the fetoplacental macrovasculature in normal pregnancies and in those complicated by fetal growth restriction. *Acta Obstet. Gynecol. Scand.* **97**, 322–329. (doi:10.1111/aogs.13289)
4. Aughwane R *et al.* 2019 Micro-CT and histological investigation of the spatial pattern of feto-placental vascular density. *Placenta* **88**, 36–43. (doi:10.1016/j.placenta.2019.09.014)
5. Junaid TO, Bradley RS, Lewis RM, Aplin JD, Johnstone ED. 2017 Whole organ vascular casting and microCT examination of the human placental vascular tree reveals novel alterations associated with pregnancy disease. *Sci. Rep.* **7**, 4144. (doi:10.1038/s41598-017-04379-0)
6. Romina Plitman M, Stephen Charnock-Jones D, Burton GJ, Oyen ML. 2016 Three-dimensional modeling of human placental terminal villi. *Placenta* **43**, 54–60. (doi:10.1016/j.placenta.2016.05.001)
7. Lisman BAM, van den Hoff MJB, Boer K, Bleker OP, van Groningen K, Exalto N. 2007 The architecture of first trimester chorionic villous vascularization: a confocal laser scanning microscopical study. *Hum. Reprod.* **22**, 2254–2260. (doi:10.1093/humrep/dem143)
8. Gough A *et al.* 2017 Biologically relevant heterogeneity: metrics and practical insights. *SLAS Discov. Adv. Sci. Drug. Discov.* **22**, 213–237. (doi:10.1177/2472555216682725)
9. Uchida S. 2013 Image processing and recognition for biological images. *Dev. Growth Differ.* **55**, 523–549. (doi:10.1111/dgd.12054)
10. Cohen AR. 2014 Extracting meaning from biological imaging data. *Mol. Biol. Cell.* **25**, 3470–3473. (doi:10.1091/mbc.E14-04-0946)
11. Jensen OE, Chernyavsky IL. 2019 Blood flow and transport in the human placenta. *Annu. Rev. Fluid Mech.* **51**, 25–47. (doi:10.1146/annurev-fluid-010518-040219)
12. Kertschanska S, Schröder H, Kaufmann P. 1997 The ultrastructure of the trophoblastic layer of the degu (*Octodon degus*) placenta: a re-evaluation of the 'Channel Problem'. *Placenta* **18**, 219–225. (doi:10.1016/s0143-4004(97)90096-5)
13. Nordsletten DA, Blackett S, Bentley MD, Ritman EL, Smith NP. 2006 Structural morphology of renal vasculature. *Am. J. Physiol. Circ. Physiol.* **291**, H296–H309. (doi:10.1152/ajpheart.00814.2005)
14. Skawina A, Litwin JA, Gorczyca J, Miodoński AJ. 1994 The vascular system of human fetal long bones: a scanning electron microscope study of corrosion casts. *J. Anat.* **185**, 369–376.
15. Townsley MI. 2012 Structure and composition of pulmonary arteries, capillaries, and veins. *Compr. Physiol.* **2**, 675–709. (doi:10.1002/cphy.c100081)
16. Atli İ, Gedik OS. 2021 Sine-Net: a fully convolutional deep learning architecture for retinal blood vessel segmentation. *Eng. Sci. Technol. Int. J.* **24**, 271–283. (doi:10.1016/j.jestch.2020.07.008)
17. Looney P, Stevenson GN, Nicolaides KH, Plasencia W, Molloholli M, Natsis S, Collins SL. 2017 Automatic 3D ultrasound segmentation of the first trimester placenta using deep learning. In *2017 IEEE 14th Int. Symp. on Biomedical Imaging (ISBI 2017), Melbourne, Australia, 18–21 April 2017*, pp. 279–282. (doi:10.1109/ISBI.2017.7950519)
18. Luo Z, Zhang Y, Zhou L, Zhang B, Luo J, Wu H. 2019 Micro-vessel image segmentation based on the AD-UNet model. *IEEE Access* **7**, 143 402–14 34–11. (doi:10.1109/ACCESS.2019.2945556)
19. Xiancheng W *et al.* 2018 Retina blood vessel segmentation using a U-Net based convolutional neural network. *Procedia Comput. Sci.* 1–11.
20. Livne M *et al.* 2019 A U-Net deep learning framework for high performance vessel segmentation in patients with cerebrovascular disease. *Front. Neurosci.* **13**, 97. (doi:10.3389/fnins.2019.00097)
21. Han M, Bao Y, Sun Z, Wen S, Xia L, Zhao J, Du J, Yan Z. 2019 Automatic segmentation of human placenta images with U-Net. *IEEE Access* **7**, 180 083–180 092. (doi:10.1109/ACCESS.2019.2958133)
22. Sadda P, Imamoglu M, Dombrowski M, Papademetris X, Bahtiyar MO, Onofrey J. 2019 Deep-learned placental vessel segmentation for intraoperative video enhancement in fetoscopic surgery. *Int. J. Comput. Assist. Radiol. Surg.* **14**, 227–235. (doi:10.1007/s11548-018-1886-4)
23. Milletari F, Navab N, Ahmadi S-A. 2016 V-Net: fully convolutional neural networks for volumetric medical image segmentation. In *2016 4th Int. Conf. on 3D Vision, Stanford, CA, USA, 25–28 October 2016*, pp. 1–11.
24. Hecksel CW *et al.* 2016 Quantifying variability of manual annotation in cryo-electron tomograms. *Microsc. Microanal.* **22**, 487–496. (doi:10.1017/S1431927616000799).
25. James JL, Whitley GS, Cartwright JE. 2010 Pre-eclampsia: fitting together the placental, immune

and cardiovascular pieces. *J. Pathol.* **221**, 363–378. (doi:10.1002/path.2719)

26. Tun WM, Yap CH, Saw SN, James JL, Clark AR. 2019 Differences in placental capillary shear stress in fetal growth restriction may affect endothelial cell function and vascular network formation. *Sci. Rep.* **9**, 9876. (doi:10.1038/s41598-019-46151-6)
27. Erlich A, Nye GA, Brownbill P, Jensen OE, Chernyavsky IL. 2019 Quantifying the impact of tissue metabolism on solute transport in feto-placental microvascular networks. *Interface Focus* **9**, 20190021. (doi:10.1098/rsfs.2019.0021)
28. Burton GJ, Woods AW, Jauniaux E, Kingdom JCP. 2009 Rheological and physiological consequences of conversion of the maternal spiral arteries for uteroplacental blood flow during human pregnancy. *Placenta* **30**, 473–482. (doi:10.1016/j.placenta.2009.02.009)
29. Perazzolo S, Lewis RM, Sengers BG. 2017 Modelling the effect of intervillous flow on solute transfer based on 3D imaging of the human placental microstructure. *Placenta* **60**, 21–27. (doi:10.1016/j.placenta.2017.10.003)
30. Alim K, Parsa S, Weitz DA, Brenner MP. 2017 Local pore size correlations determine flow distributions in porous media. *Phys. Rev. Lett.* **119**, 144501. (doi:10.1103/PhysRevLett.119.144501)
31. Dellschaft NS *et al.* 2020 The haemodynamics of the human placenta in utero. *PLoS Biol.* **18**, e3000676. (doi:10.1371/journal.pbio.3000676)
32. Pearce P, Brownbill P, Janáček J, Jirkovská M, Kubínová L, Chernyavsky IL, Jensen OE, Zenclussen AC. 2016 Image-based modeling of blood flow and oxygen transfer in feto-placental capillaries. *PLoS ONE* **11**, e0165369. (doi:10.1371/journal.pone.0165369)
33. Chernyavsky IL, Leach L, Dryden IL, Jensen OE. 2011 Transport in the placenta: homogenizing haemodynamics in a disordered medium. *Phil. Trans. R. Soc. A* **369**, 4162–4182. (doi:10.1098/rsta.2011.0170)
34. Roth CJ, Haeussner E, Ruebelmann T, Koch F, Schmitz C, Frank H-G, Wall WA. 2017 Dynamic modeling of uteroplacental blood flow in IUGR indicates vortices and elevated pressure in the intervillous space—a pilot study. *Sci. Rep.* **7**, 40771. (doi:10.1038/srep40771)
35. Choi JS *et al.* 2009 Fabrication of porous extracellular matrix scaffolds from human adipose tissue. *Tissue Eng. Part C Methods* **16**, 387–396. (doi:10.1089/ten.TEC.2009.0276)
36. Song M, Liu Y, Hui L. 2018 Preparation and characterization of acellular adipose tissue matrix using a combination of physical and chemical treatments. *Mol. Med. Rep.* **17**, 138–146. (doi:10.3892/mmr.2017.7857)
37. Torres-Sanchez C, McLaughlin J, Fotticchia A. 2018 Porosity and pore size effect on the properties of sintered Ti35Nb4Sn alloy scaffolds and their suitability for tissue engineering applications. *J. Alloys Compd.* **731**, 189–199. (doi:10.1016/j.jallcom.2017.10.026)
38. Wang S, Liu L, Li K, Zhu L, Chen J, Hao Y. 2019 Pore functionally graded Ti6Al4 V scaffolds for bone tissue engineering application. *Mater. Des.* **168**, 107643. (doi:10.1016/j.matdes.2019.107643)
39. Palaiologou E *et al.* 2017 Serial block-face scanning electron microscopy of erythrocytes protruding through the human placental syncytiotrophoblast. *J. Anat.* **231**, 634–637. (doi:10.1111/joa.12658)
40. Cunningham D, Morgan RJ, Mills PR, Nelson LM, Toner PG, Soukop M, McArdle CS, Russell RI. 1985 Functional and structural changes of the human proximal small intestine after cytotoxic therapy. *J. Clin. Pathol.* **38**, 265–270. (doi:10.1136/jcp.38.3.265)
41. Bearce EA, Grimes DT. 2021 On being the right shape: roles for motile cilia and cerebrospinal fluid flow in body and spine morphology. *Semin. Cell Dev. Biol.* **110**, 104–112. (doi:10.1016/j.semcdb.2020.07.005)
42. Brownbill P, Sebire N, McGillick E V, Ellery S, Murthi P. 2018 Ex vivo dual perfusion of the human placenta: disease simulation, therapeutic pharmacokinetics and analysis of off-target effects. In *Preeclampsia. Methods in molecular biology* (eds P Murthi, C Vaillancourt), pp. 173–189. New York, NY: Humana Press. (doi:10.1007/978-1-4939-7498-6_14)
43. Lu B, Torquato S. 1990 Local volume fraction fluctuations in heterogeneous media. *J. Chem. Phys.* **93**, 3452–3459. (doi:10.1063/1.458827)
44. Lykidis D, Van Noorden S, Armstrong A, Spencer-Dene B, Li J, Zhuang Z, Stamp GWH. 2007 Novel zinc-based fixative for high quality DNA, RNA and protein analysis. *Nucleic Acids Res.* **35**, e85–e85. (doi:10.1093/nar/gkm433)
45. Tokudome Y, Morimoto T, Tarutani N, Vaz PD, Nunes CD, Prevot V, Stenning GBG, Takahashi M. 2016 Layered double hydroxide nanoclusters: aqueous, concentrated, stable, and catalytically active colloids toward green chemistry. *ACS Nano* **10**, 5550–5559. (doi:10.1021/acsnano.6b02110)
46. Gash AE, Tillotson TM, Satcher JH, Poco JF, Hrubesh LW, Simpson RL. 2001 Use of epoxides in the sol–gel synthesis of porous iron(III) oxide monoliths from Fe(III) salts. *Chem. Mater.* **13**, 999–1007. (doi:10.1021/cm0007611)
47. Pešić ZD, De Fanis A, Wagner U, Rau C. 2013 Experimental stations at I13 beamline at diamond light source. *J. Phys: Conf. Ser.* **425**, 182003. (doi:10.1088/1742-6596/425/18/182003)
48. Rau C, Wagner U, Pešić Z, De Fanis A. 2011 Coherent imaging at the diamond beamline I13. *Physica Status Solidi* **208**, 2522–2525. (doi:10.1002/pssa.201184272)
49. Kak AC, Slaney M. 2001 *Principles of computerized tomographic imaging*. Philadelphia, PA: SIAM.
50. Atwood RC, Bodey AJ, Price SWT, Basham M, Drakopoulos M. 2015 A high-throughput system for high-quality tomographic reconstruction of large datasets at diamond light source. *Phil. Trans. R. Soc. A* **373**, 20140398. (doi:10.1098/rsta.2014.0398)
51. Strotton MC, Bodey AJ, Wanelik K, Darrow MC, Medina E, Hobbs C, Rau C, Bradbury EJ. 2018 Optimising complementary soft tissue synchrotron X-ray microtomography for reversibly-stained central nervous system samples. *Sci. Rep.* **8**, 12017. (doi:10.1038/s41598-018-30520-8)
52. Guo E *et al.* 2017 Synchrotron X-ray tomographic quantification of microstructural evolution in ice cream—a multi-phase soft solid. *RSC Adv.* **7**, 15 561–15 573. (doi:10.1039/C7RA00642J)
53. Luengo I *et al.* 2017 SuRVoS: super-region volume segmentation workbench. *J. Struct. Biol.* **198**, 43–53. (doi:10.1016/j.jsb.2017.02.007)
54. Ronneberge O, Fischer P, Brox T. 2015 U-Net: convolutional networks for biomedical image segmentation. (https://arxiv.org/abs/1505.04597)
55. Howard J, Gugger S. 2020 Fastai: a layered API for deep learning. *Information* **11**, 108. (doi:10.3390/info11020108)
56. He K, Zhang X, Ren S, Sun J. 2015 Deep residual learning for image recognition. (https://arxiv.org/abs/1512.03385)
57. Russakovsky O *et al.* 2015 ImageNet large scale visual recognition challenge. *Int. J. Comput. Vis.* **115**, 211–252. (doi:10.1007/s11263-015-0816-y)
58. Brownbill P, Mahendran D, Owen D, Swanson P, Thornburg KL, Nelson DM, Sibley CP. 2000 Denudations as paracellular routes for alpha fetoprotein and creatinine across the human syncytiotrophoblast. *Am. J. Physiol. Integr. Comp. Physiol.* **278**, R677–R683. (doi:10.1152/ajpregu.2000.278.3.R677)
59. Elias H, Hyde DM. 1980 An elementary introduction to stereology (quantitative microscopy). *Am. J. Anat.* **159**, 411–446. (doi:10.1002/aja.1001590407)
60. Rueden CT, Schindelin J, Hiner MC, DeZonia BE, Walter AE, Arena ET, Eliceiri KW. 2017 ImageJ2: ImageJ for the next generation of scientific image data. *BMC Bioinf.* **18**, 529. (doi:10.1186/s12859-017-1934-z)
61. Baddeley A, Jensen EBV. 2005 *Stereology for statisticians*. New York, NY: Chapman & Hall/CRC.
62. Oluwadebi AG, Taylor KG, Ma L. 2019 A case study on 3D characterisation of pore structure in a tight sandstone gas reservoir: the Collyhurst Sandstone, East Irish Sea Basin, northern England. *J. Nat. Gas Sci. Eng.* **68**, 102917. (doi:10.1016/j.jngse.2019.102917)
63. Zhang L, Jing W, Yang Y, Yang H, Guo Y, Sun H, Zhao J, Yao J. 2019 The investigation of permeability calculation using digital core simulation technology. *Energies* **12**, 3273. (doi:10.3390/en12173273)
64. Zhao Y, Zhu G, Zhang C, Liu S, Elsworth D, Zhang T. 2018 Pore-scale reconstruction and simulation of non-Darcy flow in synthetic porous rocks. *J. Geophys. Res. Solid Earth* **123**, 2770–2786. (doi:10.1002/2017JB015296)

A massively multi-scale approach to characterising tissue architecture by synchrotron micro-CT applied to the human placenta

W. M. Tun, G. Poologasundarampillai, H. Bischof, G. Nye, O. N. F. King, M. Basham, Y. Tokudome, R. M. Lewis, E. D. Johnstone, P. Brownbill, M. Darrow, and I. L. Chernyavsky

SUPPLEMENTARY MATERIALS

S1. SAMPLE PREPARATION

TABLE S1: Demographics and placental tissue preparation summary.

	Specimen 1	Specimen 2	Specimen 3	Specimen 4
DLS ID	123761	120077	123744	123749
Ethics (TOM) number	2654-H2	2797-F	2811-F	3079-D
Mode of delivery [a]	CS	V	CS	CS
Maternal age (years)	36	32	34	27
Parity	1	2	0	1
Gestational age (weeks+days)	39+0	37+6	35+2	39
BMI	24	29	25	30
Smoker	No	No	Yes	No
Fetal sex	Male	Male	Male	Male
Birthweight (g)	3386	2260	2082	3230
Birthweight centile (%)	49.2	0.3	4.6	29.9
Ex vivo parameters				
Cotyledon weight (g)	29	39	25	40
Fixative reagent	Z7+PFA	Z7+PFA	Z7+PFA	Z7+PFA
Contrast reagent – fetal side	Batson's	Yasuaki's	Yasuaki's	Yasuaki's
Contrast reagent – maternal side	Z7	Z7	Z7	Z7+PTA
Tissue processing [b]	CP-dried	Frozen	Wax-embed	Wax-embed

[a] CS = Cesarean; V = vaginal delivery

[b] Frozen = cryo-frozen in liquid N2 from fresh; CP-dried = ethanol dehydrated and critical-point dried; Wax-embed = ethanol dehydrated and wax-embedded

A

Biological structures of interest	Segmentation routine proposed for the various methods of obtaining X-ray contrast	
Intervillous space	**Contrast based segmentation** - Z7 fix & PTA stain	
	Machine learning assisted segmentation - Z7 fix	
Stroma (syncytio-trophoblast)	**Contrast based segmentation** - Extended Z7 fix or PTA stain	
	Machine learning assisted segmentation - Extended Z7 fix or PTA stain	
Fetal villi network	**Contrast based segmentation**	
	Vessels: Vascular corrosion casts or perfuse with contrast agent containing resins.	**Capillary**: Perfuse with a low viscous resin to avoid artificially bulging out and corrosion cast or add nano-particles to resin for contrast.
	Machine learning assisted segmentation	
	Vessels	**Capillary**
	Resin perfuse and embed tissue (tissue corrosion or incorporation of contrast agent not necessary).	

Various methods for microCT placental sample preparation

Specimen 1 - Ethanol dehydrate & critical point dry: May lead to tissue shrinkage. Sample motion from X-ray beam induced dehydration can be a potential issue when synchrotron source radiation is used. Gives the best contrast for syncytiotrophoblast.	Specimens 3 & 4 - Ethanol dehydrate & wax embed: May lead to tissue shrinkage and delamination of syncytiotrophoblast. Poor contrast between soft tissue and wax, requires phase contrast imaging.	Specimen 2 - Plunge freeze: Preserves physiological structures and is suited to imaging soft tissue. However, requires a cryo-stream or cold-stage to maintain samples under cryo-conditions during scanning.

B

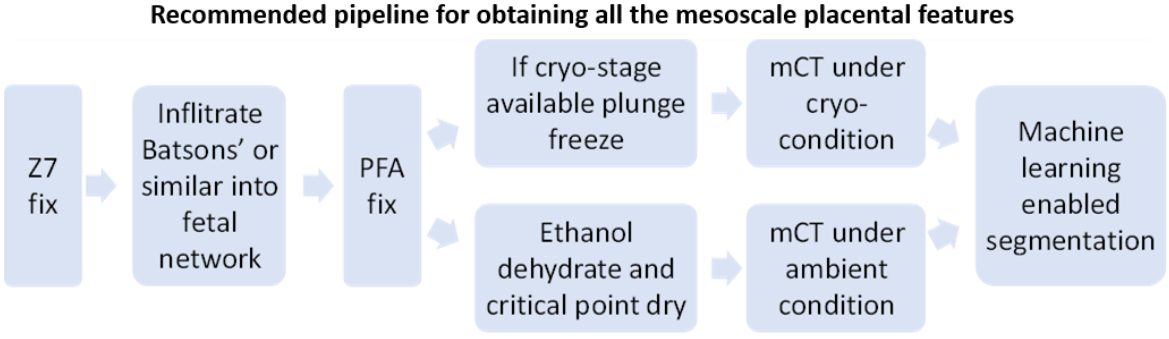

FIG. S1: Placental sample preparation required to confidently segment various features of the placenta. (A) Biological structures of interest and sample processing methods tried in this study. (B) Recommended sample processing pipelines to obtain various mesoscale placental features.

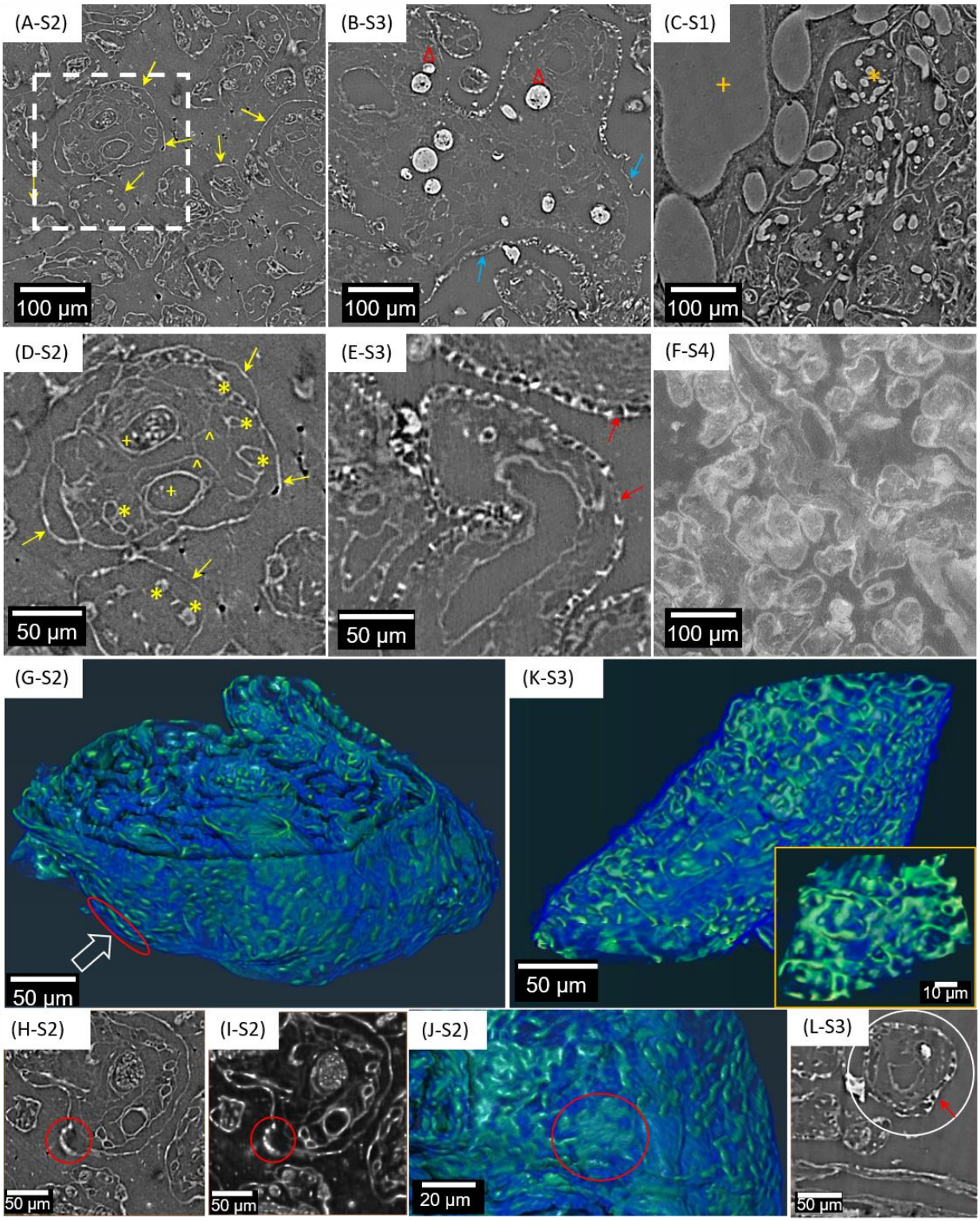

FIG. S2: Two-dimensional cross-sectional images obtained from microCT data highlighting the influence of specimen preparation on the features that can be resolved. The four specimens (labelled S1-S4; see Table S1) were imaged under three different conditions: plunge frozen in liquid nitrogen (A,D,G-J), ethanol dehydrated and wax

embedded (B,E,F,K-L) and ethanol dehydrated and critical-point dried. (C). Plunge frozen specimens were imaged using a cold stage. All specimens were Zinc-7 fixed via maternal-side perfusion. (D) Magnified image of plunge frozen specimen (white box) shows the different placental architectures of a mature intermediate villous, including a well-resolved syncytiotrophoblast (arrows in D and 3D image in G), blood vessels (+; pair of arteriole with venule where one still contains red blood cells) and various capillaries (*). It is also possible to observe a network of the stroma (^). (G,J) 3D images of plunge frozen specimen showing the thin (~3 μm) syncytiotrophoblast envelope around the villous. (H,I) 2D cross-sectional images showing aggregated nuclei within a syncytial knot (red circle and on J showing 3D image in direction indicated by a white arrow in G). Ethanol dehydrated and either wax embedded (B,E,F) or critical-point dried (C) samples were imaged at ambient temperature. Wax embedded (B) and magnified images (E,L) show blood vessels, stroma and separately resolved microvillous and syncytiotrophoblasts (red arrows). (K) 3D images of the ethanol dehydrated and wax-embedded specimen showing an intermediate villous circled in (L). Inset of (K) showing the presence of pores/open channels on the syncytiotrophoblast envelope. Further, some of the blood vessels in (B) have been perfused with the Yasuaki resin (Δ). Blue arrows on (B) show part of the syncytiotrophoblast that has delaminated from the villous. Batson's resin, which lacks an X-ray contrast agent, can be observed in (C) with better perfusion of the vessels (+) and capillaries (*). Specimen 4 (F) produces the highest X-ray contrast for stroma and trophoblast after staining with phosphotungstic acid (PTA) for 120 hours, but with poor resolution of vascular features.

S2. IMAGE SEGMENTATION

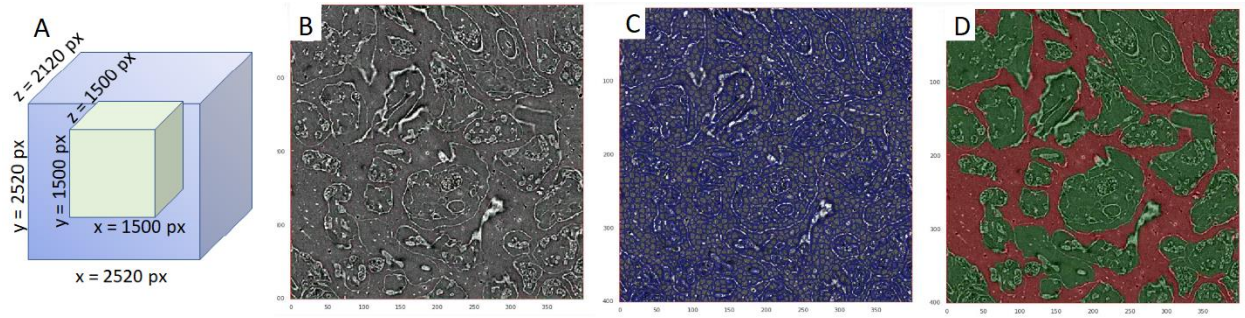

FIG. S3: Fetal tissue segmentation and validation. (**A**) The imaged tissue volume is ≈ 8 mm^3 (blue). Segmentations are of the central cropped region, with tissue volume of ≈ 1.8 mm^3 (green). (**B**) Example slice from original X-ray tomogram volume (Specimen 2). (**C**) Supervoxel regions creation based on filtered image features using SuRVoS. (**D**) Segmentation of fetal tissue and maternal IVS.

S3. FETAL VASCULAR ANALYSIS

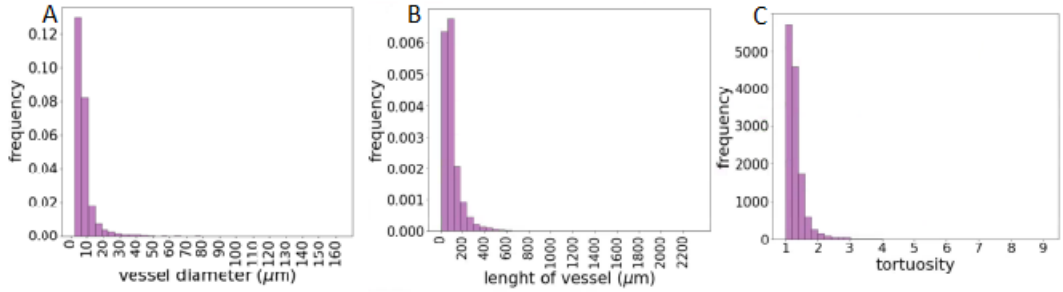

FIG. S4: Additional characterisation of fetal vascular network. Distribution of vessel (**A**) diameter, (**B**) length and (**C**) tortuosity of blood vessels from the entire vascular network from Specimen 1.

S4. MATERNAL POROUS REGION ANALYSIS

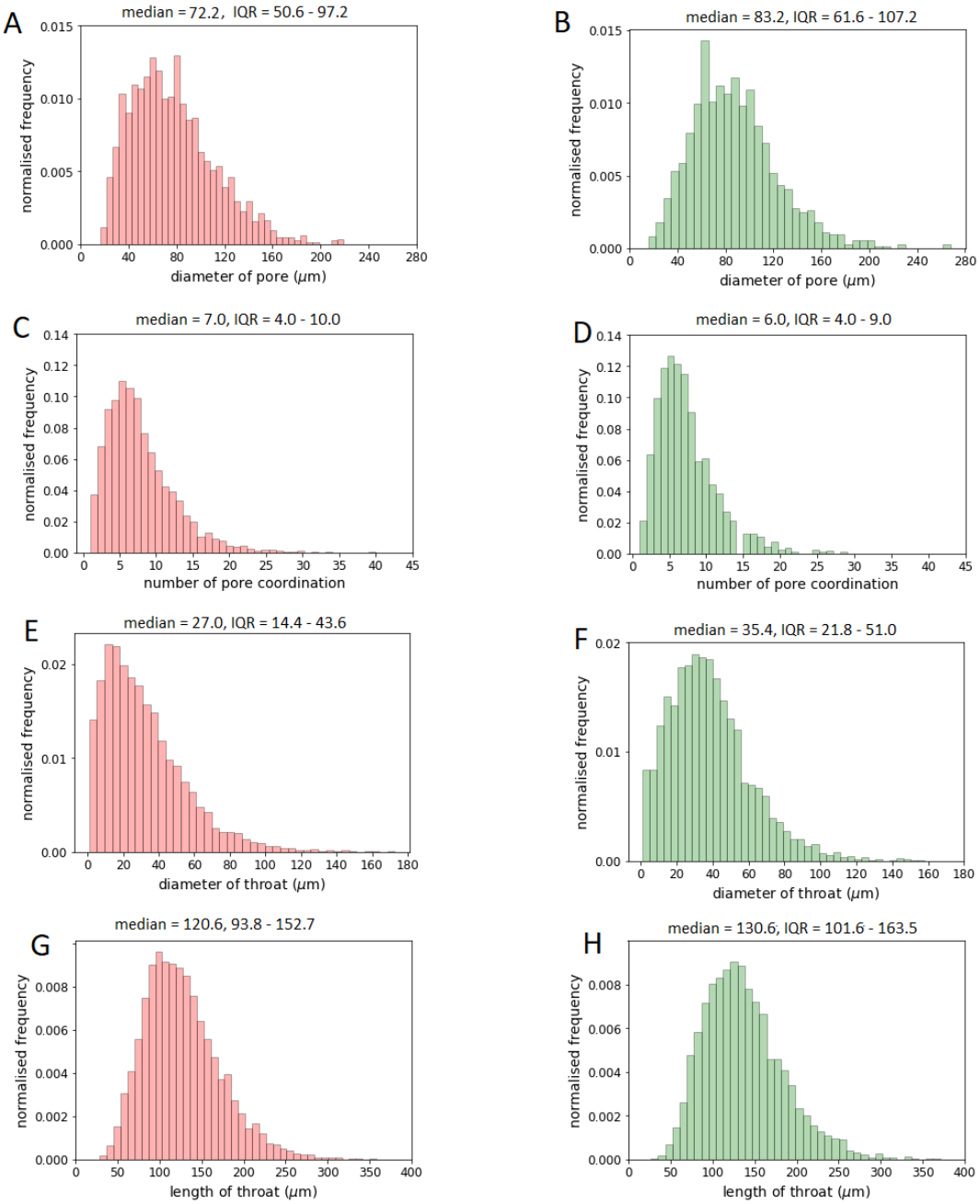

FIG. S5: Additional characterisation of maternal porous regions. Left column is specimen 1, right column is specimen 2. Distribution of (**A & B**) diameter of pores, (**C & D**) number of pore coordination, (**E & F**) diameter of throats and (**G & H**) length of throats. The median and interquartile range (in micrometer) are described on top of each graph.

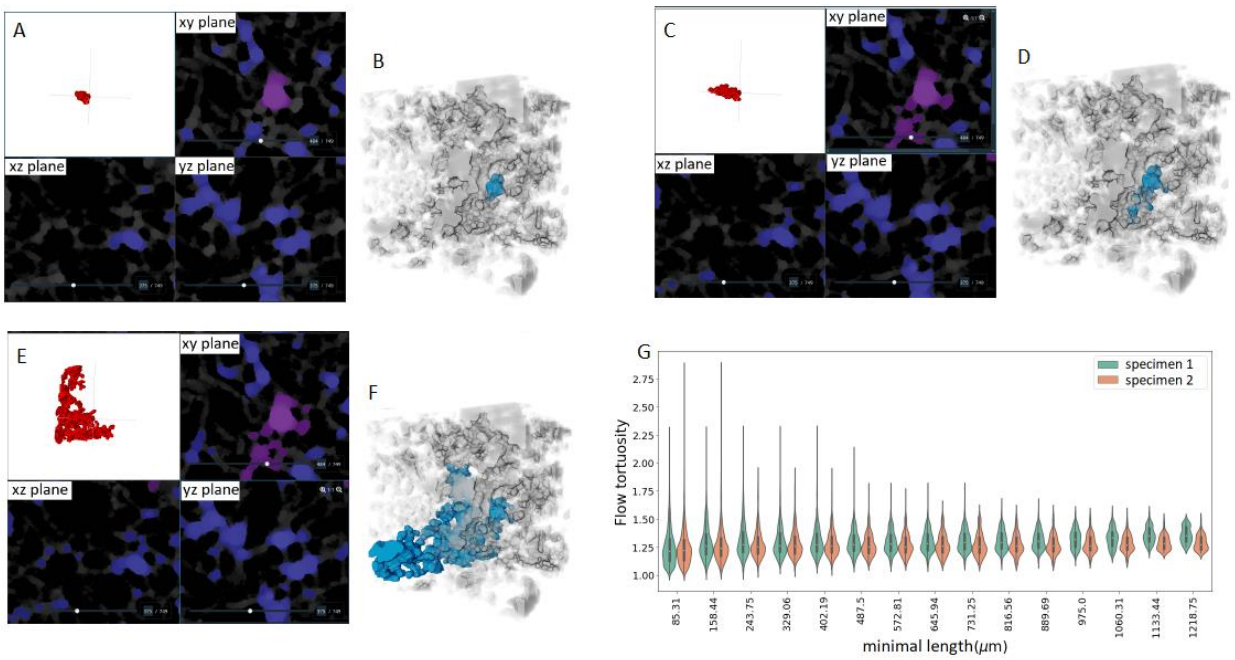

FIG. S6: Assessment of pore connectivity (A-F) and tortuosity (G). Using Specimen 2, a single pore is chosen in the tissue volume and its connectivity to other pores is limited by the diameter of the pore between (**A & B**) ≈ 48-110μm, (**C & D**) ≈ 40-110μm and (**E & F**) ≈ 37-110μm. a, c, d show the porous regions in three different planes and b, d and f show the association of porous regions with the entire volume. (**G**) Porous tortuosity (tortuosity of streamlines across the maternal IVS) measuring at various minimal lengths (of streamlines)**.**

S5. FETAL TISSUE ANALYSIS

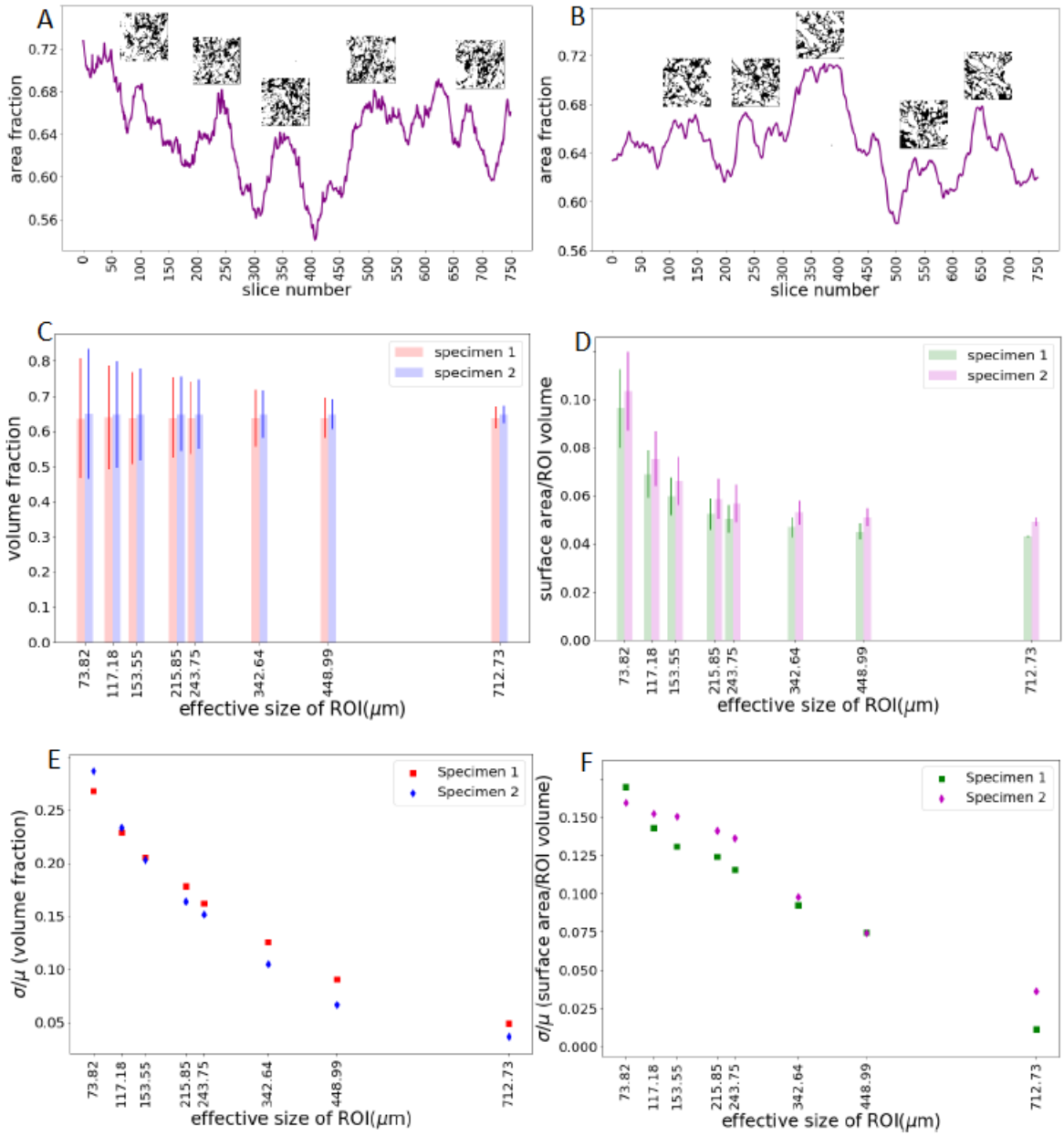

FIG. S7: Additional characterisation of fetal tissue components. (**A & B**) Area fraction variations in specimen 1 and 2. (**C**) Volume fraction vs. effective size of ROI (mean and std). (**D**) Ratio of surface area to ROI volume vs. effective size of ROI (mean and std). (**E & F**) Coefficient of variance of volume fraction and surface area/ROI volume.

S6. STEREOLOGICAL STUDY

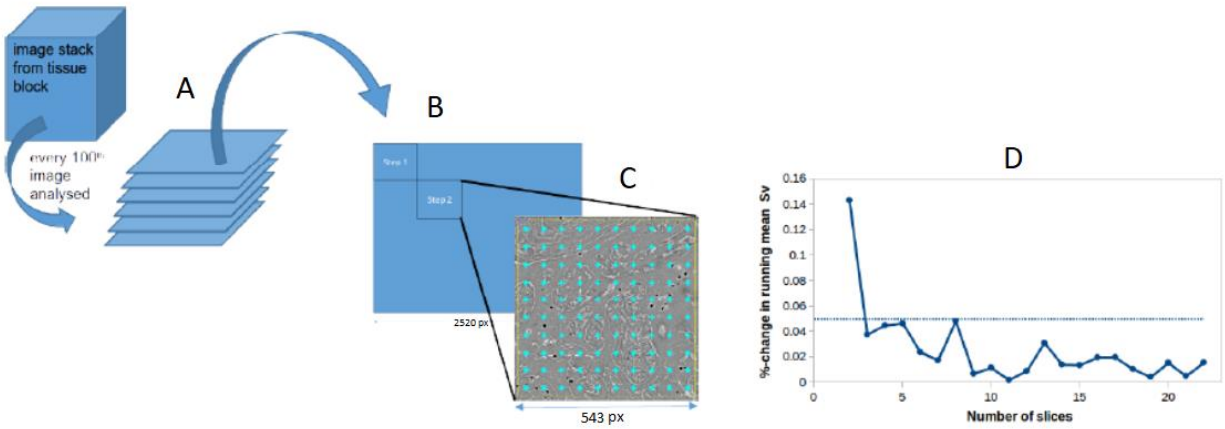

FIG. S8: Systematic sampling strategy for stereology. (**A**) Depicts the acquisition of images for analysis; (**B**) illustrates point analysis to yield volume density estimates of villi and IVS; and (**C**) shows line intersect processing to derive the surface density of the villi. Images are of a cryo-frozen human placental sample from a term FGR pregnancy. (**D**) Estimator convergence for the specific surface area (SV) of the villous tissue (analysed by stereological method from Specimen 2) with the number of slices; the dashed line denotes the 5% error level (relative change in the running mean).

S7. VALIDATION OF U-NET SEGMENTATION

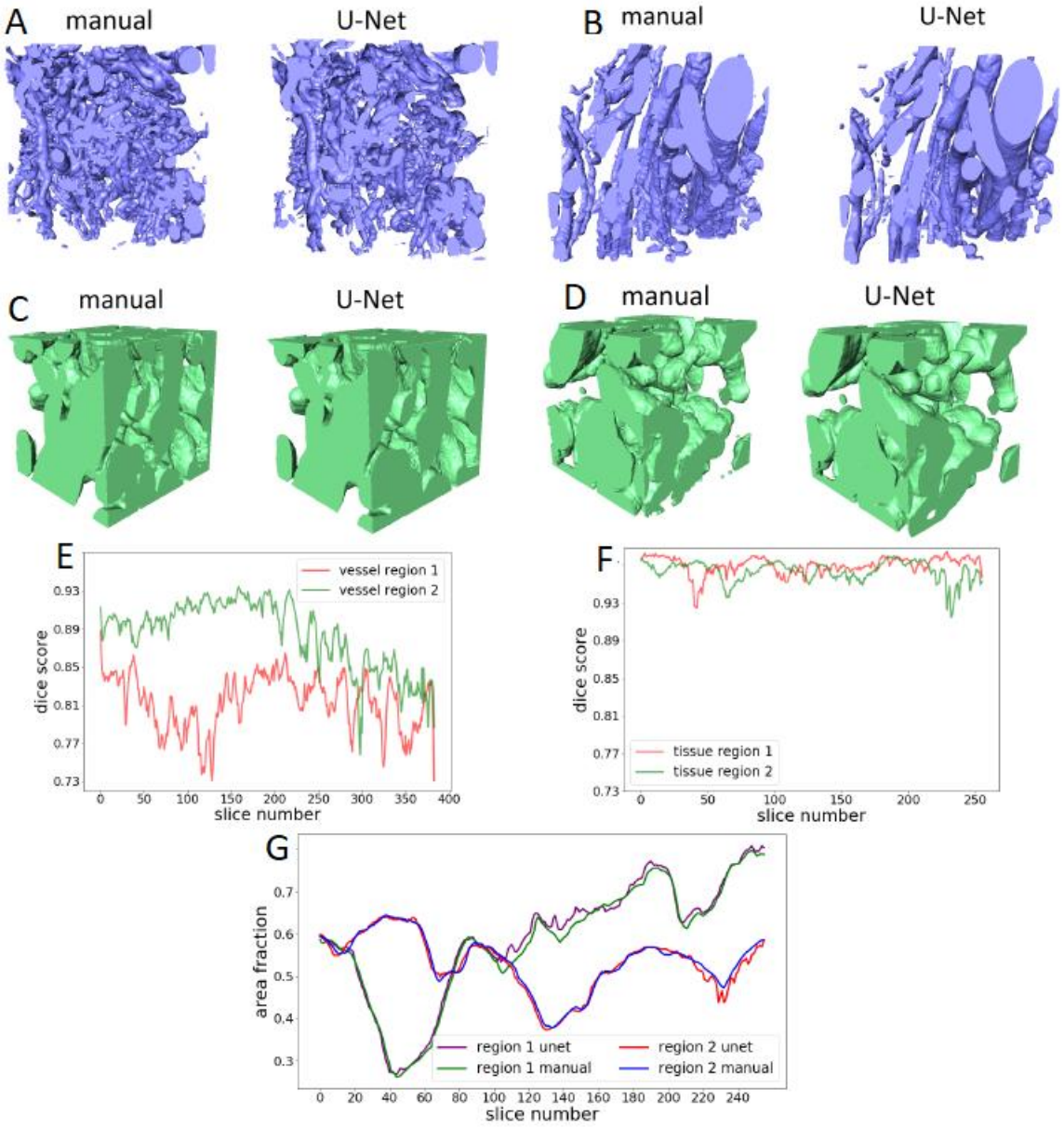

FIG. S9: Validation of U-Net segmentation of fetal vascular network and fetal tissue components. (**A & B**) Segmented volumes of vascular Region 1 and Region 2. (**C & D**) Segmented volumes of tissue Region 1 and Region 2. (**E**) Dice scores for vascular validation regions. (**F**) Dice scores for tissue validation regions. (**G**) Area fraction comparison between U-Net predictions and manual segmentations for tissue Region 1 and Region 2. All from Specimen 1.

SUPPLEMENTARY METHODS

S8. CHARACTERISTICS OF TRANSPORT IN THE INTERVILLOUS SPACE.

Let us consider a region of interest of size $L \sim 1$ mm. For typical mobile solutes such as respiratory gases and small molecules, with diffusivity $D \sim 10^{-9}\,\mathrm{m}^2/\mathrm{s}$ [1], assuming the mean intervillous space blood flow velocity U of approximately $10\,\mu\mathrm{m/s} \sim 10^{-5}\,\mathrm{m/s}$ (see Fig. 3), we have the Péclet number $Pe = U\,L/D \sim 10$, i.e. the flow contribution dominates molecular diffusion in the transport of solutes. Therefore, the pore structure, which determines the flow pathways in the intervillous space (see Figs 3 and S6), is physiologically important even for the most mobile solutes.

S9. UNCERTAINTY QUANTIFICATION OF STRUCTURAL METRICS IN A DISORDERED POROUS MEDIUM.

To characterise the scale-dependence of fluctuations in the structural metrics of a porous medium, consider a local volume fraction estimator $\hat{\phi}$ [2]

$$\hat{\phi}(\mathbf{x}) = \frac{1}{V_0} \int_{\mathscr{V}} I(\mathbf{z})\,\theta(\mathbf{z}-\mathbf{x})\,\mathrm{d}\mathbf{z}\,, \tag{S1}$$

where $I(\mathbf{x})$ is the indicator function for the phase of interest (say, the placental villous tissue; i.e. $I(\mathbf{x}) = 1$ for $\mathbf{x}$ in this phase, and is zero otherwise), and $\theta(\mathbf{x}) = \{1,\ \mathbf{x} \in \mathscr{V}_0;\ 0,\ \text{otherwise}\}$ is the indicator function for the observation region of interest (ROI) $\mathscr{V}_0$ of volume V_0, which is centred at an arbitrary location $\mathbf{x}$ within a larger porous medium domain $\mathscr{V}$.

For an ergodic and isotropic medium, $\hat{\phi}$ is shown to be an unbiased estimator, with $\mathbb{E}[\hat{\phi}] = \phi$, and the square root of normalized variance (termed 'coarseness') is given by [2]

$$\frac{\sigma_{\hat{\phi}}}{\phi} = \frac{1}{\phi\,V_0}\left[\int_{\mathscr{V}} \left[S_2(\mathbf{r}) - \phi^2\right]\,V_{\mathrm{int}}(\mathbf{r})\,\mathrm{d}\mathbf{r}\right]^{1/2}, \tag{S2}$$

where $S_2(\mathbf{r}) = \mathbb{E}[I(\mathbf{x})I(\mathbf{x}+\mathbf{r})]$ is the two-point probability function, which approaches the value of ϕ^2 for sufficiently large r, and $V_{\mathrm{int}}(\mathbf{r})$ is the intersection volume of two ROIs separated by the distance r, which depends both on the ROI size and on its shape [2].

Following Torquato *et al.* [2, 3], in the limit of sufficiently large ROI volumes (i.e. when the ROI size L is much larger than the intrinsic correlation lengthscale λ, such that $S_2(\lambda) \approx \phi^2$), the long-range structural correlations become negligibly small, and the integral (S2) reduces to an integral

in the vicinity of $r \leq \lambda$. In this case, the intersection volume $V_{\text{int}} \approx V_0\,(1 - \mathcal{O}(\lambda/L))$ approaches the volume V_0 of the ROI, and (S2) gives an asymptotic relationship

$$\frac{\sigma_{\hat{\phi}}}{\phi} \sim {V_0}^{-1/2}\, f(\phi, \lambda)\,. \tag{S3}$$

Similarly, we introduce an estimator $\hat{s}$ for the specific surface area s of the tissue phase:

$$\hat{s}(\mathbf{x}) = \frac{1}{V_0} \int_{\mathscr{V}} |\nabla I(\mathbf{z})|\, \theta(\mathbf{z} - \mathbf{x})\; \mathrm{d}\mathbf{z}\,, \tag{S4}$$

where $|\nabla I(\mathbf{x})|$ is the characteristic function for the interface, defined in the sense of generalised functions [3, 4], so that $\mathbb{E}[|\nabla I(\mathbf{x})|] = s$. Utilising the surface-surface probability function $F_{ss}(\mathbf{x}) = \mathbb{E}[|\nabla I(\mathbf{x})|\,|\nabla I(\mathbf{x}+\mathbf{r})|]$ ($F_{ss} \to s^2$ as $r \to \infty$) [4], and assuming an ergodic statistically homogeneous porous medium, we extend the technique of Lu and Torquato [2] to derive an analogous to (S2) relative variability for the specific surface area:

$$\frac{\sigma_{\hat{s}}}{s} \;=\; \frac{1}{s\,V_0} \left[\int_{\mathscr{V}} \left[F_{ss}(\mathbf{r}) - s^2 \right]\; V_{\text{int}}(\mathbf{r})\; \mathrm{d}\mathbf{r} \right]^{1/2}\,, \tag{S5}$$

where $\sigma_{\hat{s}}^2 \equiv \mathbb{V}\mathrm{ar}[\hat{s}]$.

By taking the limit of large ROI volumes for an isotropic and homogeneous porous medium, i.e. for the ROI size $L \gg \lambda_s$, we have $F_{ss}(\lambda_s) - s^2 \approx 0$ and $V_{\text{int}} \approx V_0$, and thus the relationship (S5) can be approximated by

$$\frac{\sigma_{\hat{s}}}{s} \sim {V_0}^{-1/2}\, g(s, \lambda_s)\,, \tag{S6}$$

where, similarly to (S3), the relative magnitude of the fluctuations drops as $V_0^{-1/2}$, with a factor that only depends on the correlation lengthscale and the expectation of the specific surface area.

---

[1] Erlich A, Pearce P, Mayo RP, Jensen OE, Chernyavsky IL. 2019 Physical and geometric determinants of transport in fetoplacental microvascular networks. *Sci Adv* **5**, eaav6326.

[2] Lu B, Torquato S. 1990 Local volume fraction fluctuations in heterogeneous media. *J Chem Phys* **93**, 3452–3459.

[3] Coker DA, Torquato S. 1995 Extraction of morphological quantities from a digitized medium. *J Appl Phys* **77**, 6087–6099.

[4] Doi M. 1976 A new variational approach to the diffusion and the flow problem in porous media. *J Phys Soc Jpn* **40**, 567–572.